TÉCNICO LISBOA

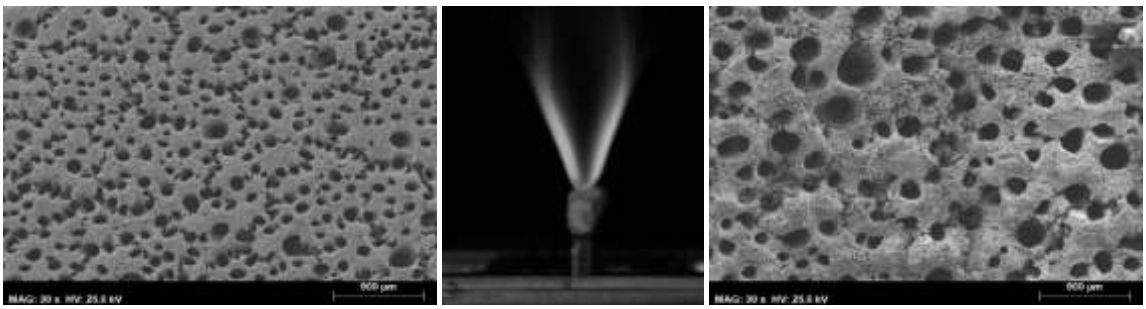

The Influence of Burner Surface Morphology on Flame Stabilization

Safira da Silva Braz

Thesis to obtain the Master of Science Degree in

Mechanical Engineering

Supervisors: Prof. Edgar Caetano Fernandes

Dr. Luísa Maria Leal da Silva Marques

Examination Committee

Chairperson: Prof. Carlos Frederico Neves Bettencourt da Silva

Supervisor: Prof. Edgar Caetano Fernandes

Member of the Committee: Prof. Teodoro José Pereira Trindade

November 2018

ACKNOWLEDGMENTS

This thesis represents the closing and, simultaneously, the beginning of a new chapter in my life. Certainly, it was a very special and enriching experience which I will always be very grateful for.

Firstly, I would like to express my gratitude to my two supervisors. Professor Edgar for all his postive attitude, time, enthusiasm and continuous support throughout this work. Dr. Luísa Marques for all the help, knowledge, care and patient during the long hours in the chemistry laboratory. And, to my laboratory colleagues that always helped me, an enormous thank you.

Also, to my closest and adorable friends Ana, Carol, Vera, Sara, Jessica, Carol and Eli for the long conversations, giving me support, motivation and good vibes. You will always be in my heart.

To my family, specially to my aunt Aldina. Her advices, incredible knowledge and beautiful words that always inspired me. Thank you!

I also a special thank to my boyfriend, Nuno. You are a wonderful human being with an enormous heart and kindness. Your emotional support was crucial to reach the end of this journey. Thank you for your time, patient, love and delicious food! Also, a huge thank you to his family.

To my mother and brother, I will always be thankful. Thank you mom, for guiding me as a person and help me complete my academic journey while providing emotional and financial support. And you brother, Nuno, for all the care, advice and encouragement in all my pursuits, and for inspiring me to follow my dreams. Despite being away, you always have been in my thoughts.

And finally, I dedicate this thesis in memory to my father, who has always believed in me and supported my search for a fulfilling career. His memory will forever remain in my heart.

RESUMO

O presente trabalho investiga a influência de superfícies de óxido de zinco (ZnO) com morfologia porosa na estabilização de chamas invertidas de pré-mistura ar-metano, em regime pobre.

A síntese do material de ZnO foi realizada através da técnica de electrodeposição *Dynamic Hydrogen Bubble Template* (DHBT) sob condições específicas de crescimento, obtendo-se diversas configurações de material (não poroso e poroso). Cada morfologia sintetizada foi caracterizada estrutural e morfologicamente, avaliando-se a influência dos vários parâmetros de electrodeposição (solução electrolítica, tempo e densidade de corrente) no desenvolvimento e formação de material poroso. Desta técnica resultaram seis amostras de ZnO poroso com uma dimensão média de diâmetro de poros na gama dos 87 e 193 µm.

Todo o material de ZnO poroso foi testado como superfície estabilizadora num queimador de dupla fenda para um intervalo de velocidades de escoamento (U) de 0,43 a 3,02 m/s. A análise experimental englobou técnicas de fotografia para visualização directa da chama e medições de temperatura da superfície com recurso a uma câmara termográfica.

Os resultados mostram que para superfícies com um diâmetro de poros superior a 167 µm, a chama extingue-se para razões de equivalência (ϕ) mais elevadas quando comparado com uma superfície sem material depositado. Particularmente, foi registada uma variação do campo de velocidades para baixas velocidades (U<1,71m/s). Esta variação obriga a base da chama a aproximar-se da superfície de ZnO, uma nova estabilização ocorre, e consequentemente, há um aumento da transferência de calor para o material de ZnO.

Palavras-Chave: Superfícies Porosas de Óxido de Zinco, Electrodeposição, Chama Invertida, Estabilidade de Chama, Câmara Termográfica, Dimensão dos Poros, Transferência de Calor

ABSTRACT

The present work studies the influence of zinc oxide (ZnO) material with a porous morphology in the stabilization of an inverted air-methane flame, in lean conditions.

The synthesis of ZnO material was done using the electrodeposition technique Dynamic Hydrogen Bubble Template (DHBT) under specific growth conditions, which produced different types of material configurations (non-porous and porous). Each synthesised material was characterized structural and morphologically, assessing the influence of the electrodeposition parameters (electrolytic solutions, time and current density) on growth of the porous material. As resulted of this technique six ZnO porous samples were obtained with a range of mean diameter porous size of 87 and 193 µm.

All ZnO porous material was tested as a stabilization surface in a twin-slit burner with a working mixture velocity (U) range of 0,43 to 3,02 m/s. The experimental analysis included photography method for flame's direct visualization and temperature measurements using a thermographic camera.

The results show that for surfaces with porous diameter greater than 167 µm, occurs the flame blow-off for higher equivalence ratios (ϕ) when compared with a surface without deposited material. Particularly it has been recorded a change in the velocity profile for lower velocities (U< 1,71 m/s). This variation forces the approximation of flame base to the ZnO surface, a new stabilization occurs and consequently an increase of the heat transfer to the ZnO material.

Keywords: Zinc Oxide Porous Material, Electrodeposition, Inverted Flame, Flame Stability, Thermographic Camera, Pores Dimension, Heat Transfer

CONTENTS

LIST OF FIGURES

LIST OF TABLES

LIST OF ACRONYMS

3D	Three dimensional
DHBT	Dynamic Hydrogen Bubble Template
EDS	Energy-dispersive X-ray Spectroscopy
IR	Infra-red
LHV	Low Heating Value
SEM	Scanning Electron Microscopy
SLPM	Standard Litres Per Minute
SS	Stainless Steel
STP	Standard Temperature and Pressure
PIV	Particle Image Velocimetry

LIST OF SYMBOLS

ROMAN SYMBOLS

c_p	Specific Heat
Dm	Mean Diameter
ds	Stand-off Distance
e	Relative Error
h	Height
h_{in}	Enthalpy Entering
i	Current Density
k_{cond}	Thermal Conductivity
L	Channel Length
U	Flow Velocity
Pe	Peclet Number
Q	Heat Flux
Re	Reynolds Number
S_L	Laminar Flame Speed
T	Temperature
T_{ad}	Adiabatic Flame Temperature
T_{amb}	Ambient Temperature
*T*atm	Atmosphere Temperature
Tobj	Object Temperature
t	Electrodeposition Time
t_{FH}	Flame Holder Thickness
W	Power Emitted
w	Width

GREEK SYMBOLS

δ_Z	Zeldovich Flame Thickness
ϕ	Equivalence Ratio
ξ	Uncertainty
ρ	Density
υ	Kinematics Viscosity

CHEMICAL SPECIES

Al_2O_3	Aluminium Oxide
CH_4	Methane
Cl	Chlorine
CO_2	Carbon Dioxide
Co_3O_4	Cobalt Oxide
CO	Carbon Monoxide
CuCrO4	Cooper Chromate
K	Potassium
KCl	Potassium Chloride
NH_4Cl	Ammonium Chloride
NOx	Nitrogen Oxides
Pd	Palladium
Pt	Platinum
Rh	Rhodium
Zn	Zinc
$ZnCl_2$	Zinc Chloride
$ZnCrO_4$	Zinc Chromate
ZnO	Zinc Oxide

CHAPTER 1

INTRODUCTION

1.1 BACKGROUND AND MOTIVATION

Emission of Nitrogen Oxide (NOx) gases have a vast effect on human health and the environment [1]. Regulations introduced in the past decades [1] have pushed industries relying on hydrocarbons combustions to improve their processes and reduce emissions. A mean to achieve this has been to use devices operating under lean fuel conditions, as they require low flame temperatures and enable reduction in NOx formation [2]. However, lean regimes promote poor flame stability which might compromises the device operation.

Also, a growing trend to microscale combustion technologies has been observed in the past few years, especially due to the rising demand for portable power generation suitable to use in micro air vehicles or in communication devices [3]. These types of portable devices strongly rely on batteries, which have a very low energy density, lack of compact, lifetime and light weight. Due these limitations, hydrocarbon's fuel appears as an alternative since they have a very high specific energy (45 MJ/Kg over 1,2 MJ/Kg of the lithium batterie) [4].

However, this scale down carries out news challenges, particularly on the micro chamber. As combustion volumes are reduced, issues of residence time, heat losses, air/fuel mixing and flame quenching become significantly relevant [5]. Surface-induced catalytic reaction has shown significant improvements in sustainable combustion in micro combustion [5]. Coating the wall surface of a combustor with a proper catalyst can lower the reaction activation energy enhancing the reaction rate in low temperatures. Consequently, the lower temperatures enabled in the process will allow NOx emission reduction [5].

In the case of methane (CH_4) combustion, metal oxides (as Co_3O_4, $ZnCrO_4$ and CuCrO4) and noble metals such as Pt, Rh and Pd have been tested and used as a promotor for catalytic oxidation of CH_4 [6]. Also, the catalysts are usually dispersed on a support. This support substrate has a porosity

above 50% and a high surface area, required characteristics for the catalytic combustion. Monoliths and ceramic honeycombs are examples of support materials used for methane catalytic reaction [6,7,8].

The support substrate plays a relevant role on the catalytic reaction, since it might influence the activity and long-term stability of the catalysts [6] and also offers high combustion efficiencies [5]. Such features are favourable for catalytic combustion application for sustaining flame in a smaller volume.

1.2 V-SHAPED FLAMES APPLICATIONS

The domestic heating industry relies heavily in exposed combustion approaches – lean and micro combustion. An example, used in house water heater equipment's, is the lamella type burner which works with a rich-lean flame interaction [9,10]. This technology is characterized by the combination and interaction of small-scale inverted flames, (Figure 1), in which a rich pilot flame is introduced in order to anchor the lean flame and consequently increase the flame stability. V-shaped flame is also an alternative designation for inverted flames.

Inverted flames burners were firstly used by Lewis and von Elbe [11], using a wire mounted in the axes of a cylindrical burner tube, and later by Edmondson and Heap [12], using stabilized V-flames and twin-slit burners in thin plates of different thicknesses, as seen in Figure 1.

In relation with catalytic combustion on domestic heating industry, works are only found which take natural gas boilers using a metal honeycomb partly coated with a catalyst [13,14]. However, these researches are focussed on the catalyst influence in combustion rate and less over the importance of the support material.

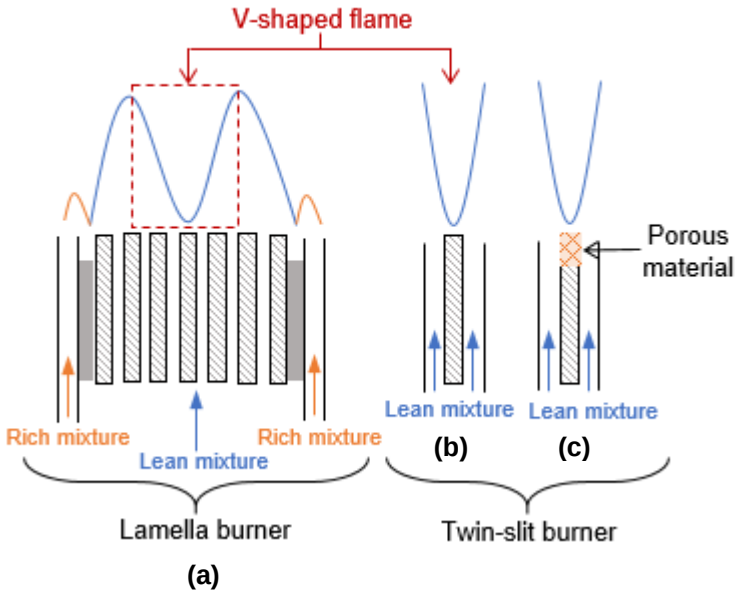

Figure 1 – Inverted flames applications: (a) lamella burner, (b) twin-slit burner and (c) twin-slit burner with porous material applied. Adapted from [9].

1.3 OBJECTIVE AND CONTRIBUTION

This study attempts to look at the potential application of catalytic surfaces in lamella burners (Figure 1(c)), in particularly for household heating market where there has been limited research. The focus has been in understanding how a porous catalyst might influence the flame behaviour, rather than looking at methane catalyst coatings. At this small scale, the morphology of a support material is of an extreme significance as the pore dimensions may introduce undesired instabilities in the flame, even with the impregnation of methane catalysts.

Study of the support morphology was achieved by producing a material with a 3D interconnected porosity, similar as the support material catalyst [8]. Zinc Oxide (ZnO) was used to synthesize the porous materials due to its low cost, high availability and low toxicity [15]. Electrodeposition as used to fabricate the porous structures as ir offered a simple, fast and low-cost process [15,16].

Notice, that this work also contemplates a chemical research about the growth mechanism and formation of porous structure from ZnO, for lamella burner applications. Electrodeposition variables it will be detailed analysed in order to understand in the favourable conditions to synthesize a porous morphology.

The next two sections will give an overview of the ZnO properties and the electrodeposition method for surface treatment.

1.4 ZINC OXIDE

Due particularly to the its semiconducting and piezoelectric properties, ZnO has been an attractive material in the field of nanotechnology leading to developments in biosensors and optoelectronics devices [17]. Additionally, due its chemical qualities, has a simple crystal-growth technology, which allows a lower fabrication cost when compared with other semiconductors used in nanotechnology [18].

ZnO is very simple to produce, is a non-toxic material and can growth in a variety of nanostructures morphologies using low cost processes. Some of the ZnO morphologies includes nanowires, nanorods and honeycomb-like structures [18].

All these advantages have contributed to a wide range of research on ZnO, in particularly in growth mechanisms [19,20,21], which have been significant to the present study and helped produce the desired 3D interconnected porous materials.

1.5 ELECTRODEPOSITION BY DYNAMIC HYDROGEN BUBBLE TEMPLATE

Electrodeposition involves the passage of a potential (or current) to reduce metal ions dissolved in an aqueous solution or ionic liquid onto a conductive substrate, as expressed by the follow chemical reaction (1),

$$M^{z+}(aq) + ze^- \rightarrow M(s) \quad [1]$$

$$Zn^{2+}(aq) + 2e^- \rightarrow Zn(s) \quad [2]$$

Chemical reaction (2) is regarding to the ZnO deposition, indicating the number of electrons that are required for the Zn reduction.

When applied the right potential (or current) a dynamic template can be obtained, since during the electrodeposition process H^+ is reduced to H_2, producing H_2 bubbles that interfere on solid growth mechanism. This spontaneous process, known as Dynamic Hydrogen Bubble Template (DHBT), occurs during the metal deposition which allows to produce easily porous morphologies [22].

It is important to understand that the source of H^+ present in DHBT is coming from the aqueous solution – electrolyte – where it is also the metal species that will be deposited onto the substrate – electrode.

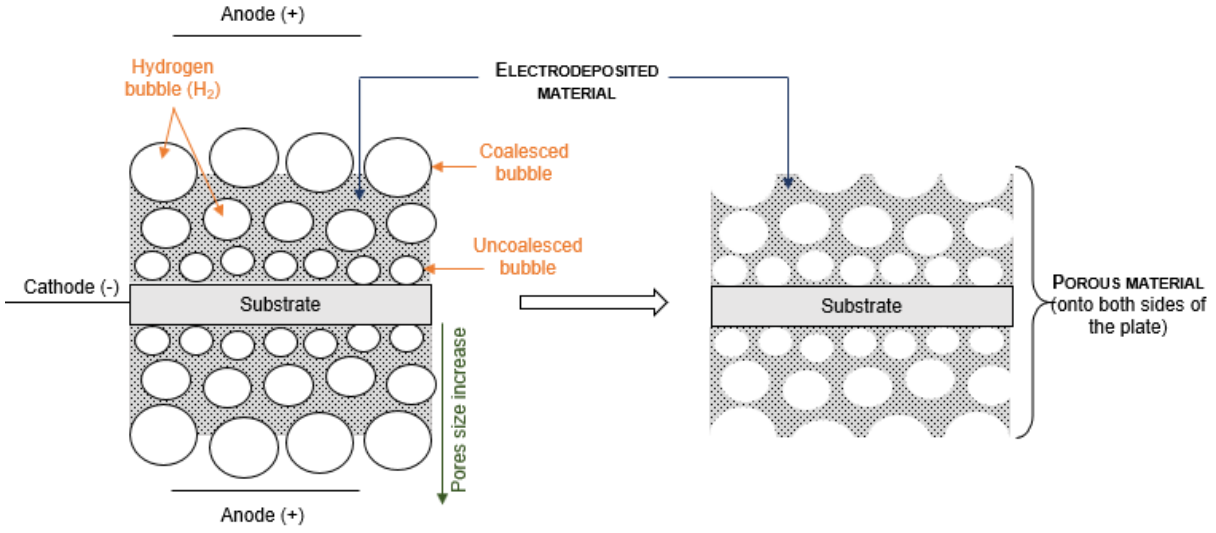

Figure 2 – Scheme demonstrating the hydrogen bubbling acting as template in the production of a porous material deposited on SS plates. Adapted from [15].

Figure 2 shows a schematic representation of the DHBT mechanism, showing that the material deposition occurs under intense hydrogen evolution [22]. Also, the metal electrodeposition occurs around the bubbles which lead to a production of pores with the same size as the release diameter of the bubbles [22]. In fact, the larger pore size as the film grows is explained by the increased coalescence of bubbles [22]. Electrolyte solution, deposition time (*t*) and current density (*i*) are parameters that can be changed during this process.

Flexibility, quickness and cheapness are the main features of this technique, turning it to the most used process in porous material production [15].

1.6 THESIS OUTLINE

This thesis is organized in four chapters. The present chapter provides an introductory contextualization of combustion areas where this work is related, a literature review on the subject and describe the motivation and objectives of the thesis. Also, this section includes a brief explanation of the chemical method used in order to clarify some aspects that might be outside of the knowledge of mechanical area.

The chapter 2 depicts the experimental apparatus used for both combustion tests and for chemical laboratory where was synthesize the desired ZnO materials. It also includes the equipment's used, the data treatments methods and an uncertainty analysis.

All the results and discussions are presented in chapter 3. This chapter is divided into two main groups: one for ZnO materials study and other for the combustion tests analysis. In ZnO material group is described all the obtained morphologies and the ZnO porous materials preservation after performing the combustion tests. Flame stability analysis, temperature evolution, stand-off distances and heat transfer results are discussed in the second group of chapter 3.

The closing chapter lists the most insights from this thesis and suggest future works based on the obtained results.

CHAPTER 2

EXPERIMENT

2.1 BURNER CHARACTERIZATION

A two-dimensional slit burner was used with two rectangular channels with equal geometry of size 40x2 mm (height (*h*) and width (*w),* respectively*)*. Methane (CH_4) was used as the fuel for all tests. The flame was stabilized behind the trailing edge of a plate with a 3mm thickness (*t*), which was positioned a 13 mm above the burner exit (Figure 3). This type of burner configuration allows to produce and isolate a V-shaped flame, giving improved optical access during experiments.

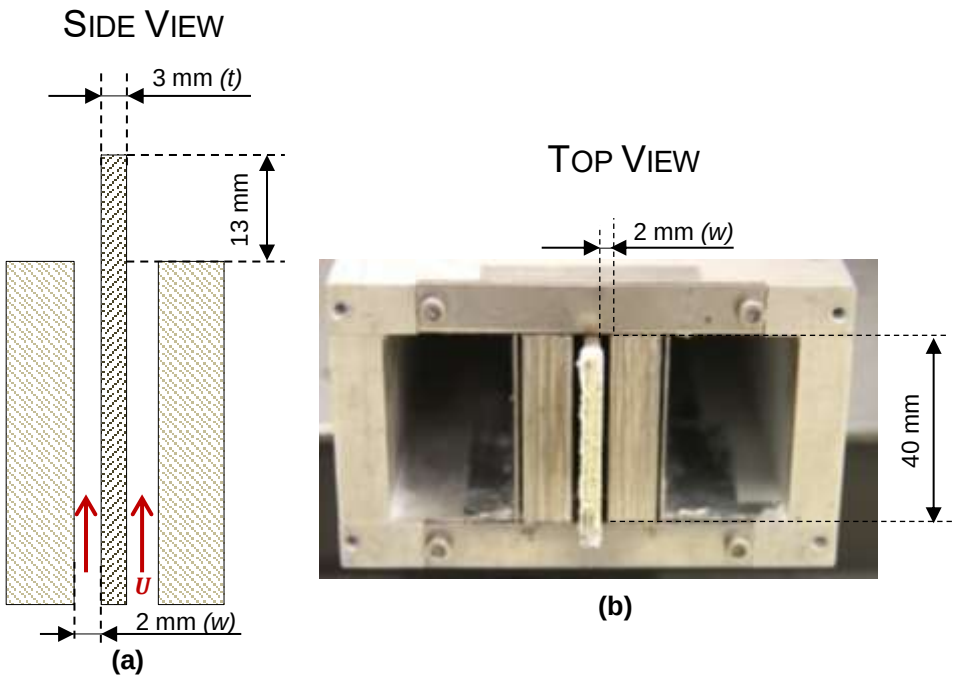

Figure 3 – Burner schematic view: (a) side view where U_L is representing the lean mixture velocity and (b) original top view with ZnO porous material deposited plate installed.

Figure 4 shows the experimental setup. The system was feed by two main streams, one of methane and another of air (Figure 5). The methane was supplied by a high-pressure cylinder and the air removed directly from the atmosphere, passing by an air filter to ensure the removal of impurities and water before continuing its course. Each stream was connected to a digital Alicat mass flow meter (Alicat Scientific, 16 Series) which can be controlled using the flow meters' software to set the desire conditions. After passing through the flow controllers, both air and methane streams were mixed and plugged to the twin-slit burner. This scheme allows the user to control both flow meters imposing the equivalence ratio (ϕ) as well the velocity at burner exit (U).

The maximum capacity of controllers for CH_4 and air were 5 and 50 standard litters per meter (SLPM), respectively. According the manufacture the controller calibration has an average error equivalent to 0.8% of the flow measured over 0.2% of its full scale. Also, the controllers' program was developed using the LabVIEW application by National Instruments.

It should be emphasized that the plates used in burner tests were plates coated with synthesized ZnO porous materials. Tests were also performed with a clean stain steel (SS) plate used as a reference sample for comparison with produced materials

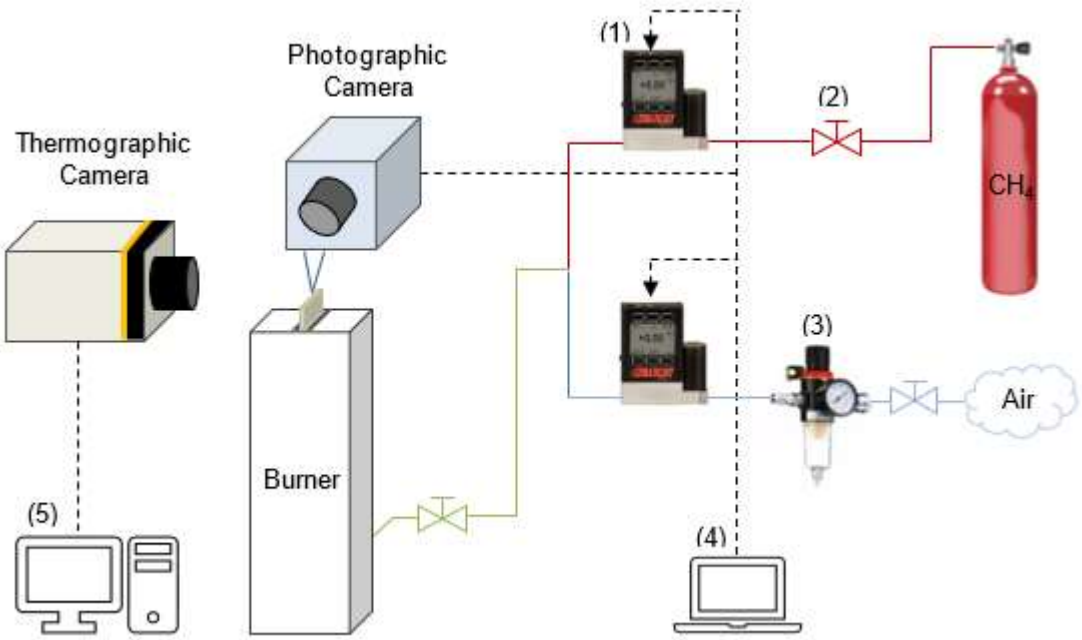

Figure 4 – Experimental arrangement with thermographic camera position and gas supply system where: (1) Alicat flow meters, (2) manual on/off valve, (3) pressure gauge and air filter regulator, (4) control and data acquisition and (5) data acquisition (temperatures).

2.1.1 BURNER VARIABLES

The flow velocity (U) was controlled manipulating the Reynolds Number, Re, in the controllers' program. U [m/s] is obtained from Re [-] as expressed in Equation (1).

$$R_e = \frac{UL}{\nu} \tag{1}$$

where, L is the channel length [m] and ν is the mixture's kinematic viscosity [m^2/s].

The equivalence ratio (ϕ), expressed in Equation (2), is defined as the ratio between the molar quantities of fuel (CH_4) and air, normalized by the same ratio at stoichiometric conditions.

$$\phi = \frac{n_{CH_4}/n_{air}}{(n_{CH_4}/n_{air})_{st}} \tag{2}$$

in which, n_{CH_4} and n_{air} corresponds to the number of moles of CH_4 and air, respectively. The suffix *st* stands for stoichiometric conditions.

Table 1 depicts the used fluids properties for Standard Temperature and Pressure (STP) conditions.

Table 1 – Methane and air properties in STP.

Property	CH4	Air
ρ [Kg/m^3]	0.66	1.18
μ x 10^{-6} [Pa.s]	11.19	18.46
M [kg/k.mol]	16.04	2896
LHV [MJ/Kg]	50.01	-

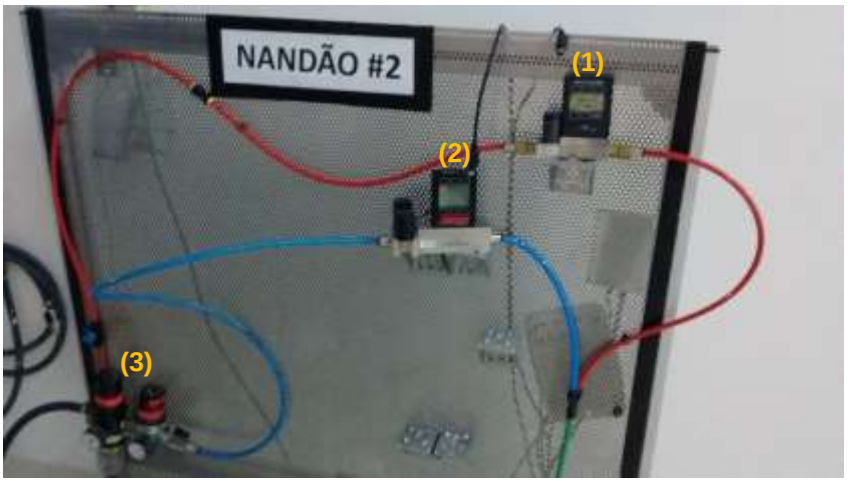

Figure 5 – Flow meters installation: (1) methane stream (Q_{max} = 5 SLPM), (2) air stream (Q_{max} = 50 SLPM) and (3) pressure gauge and air filter regulator.

2.2 TEMPERATURE MEASUREMENTS

Figure 6 shows the experimental setup used for temperature measurements. The temperatures were measured using a ONCA 4969 infrared (IR) thermographic camera from Xenics, operating at the temperature range of 40-400˚C. Table 2 depicts the main characteristics of the used camera.

Table 2 – Thermographic camera characteristics

Camera Characteristics	Optical System	Image Characteristics
Sensor: InSb (MWIR)	Focal lens: 13 mm	Video rate: 60 Hz
Spectral sensibility 3,5 to 5µm	Optics material: Germanium	Max. framerate: 3000 fps
Resolution: 320x256 pixels		Minimum region of interest (ROI): 15x5 pixels
Pixel dimension: 30x30 µm		Exposition time > 1µs
Refrigeration: Stirling engine		
Thermal sensibility < 17 mk		
Pixel operability > 99,5%		

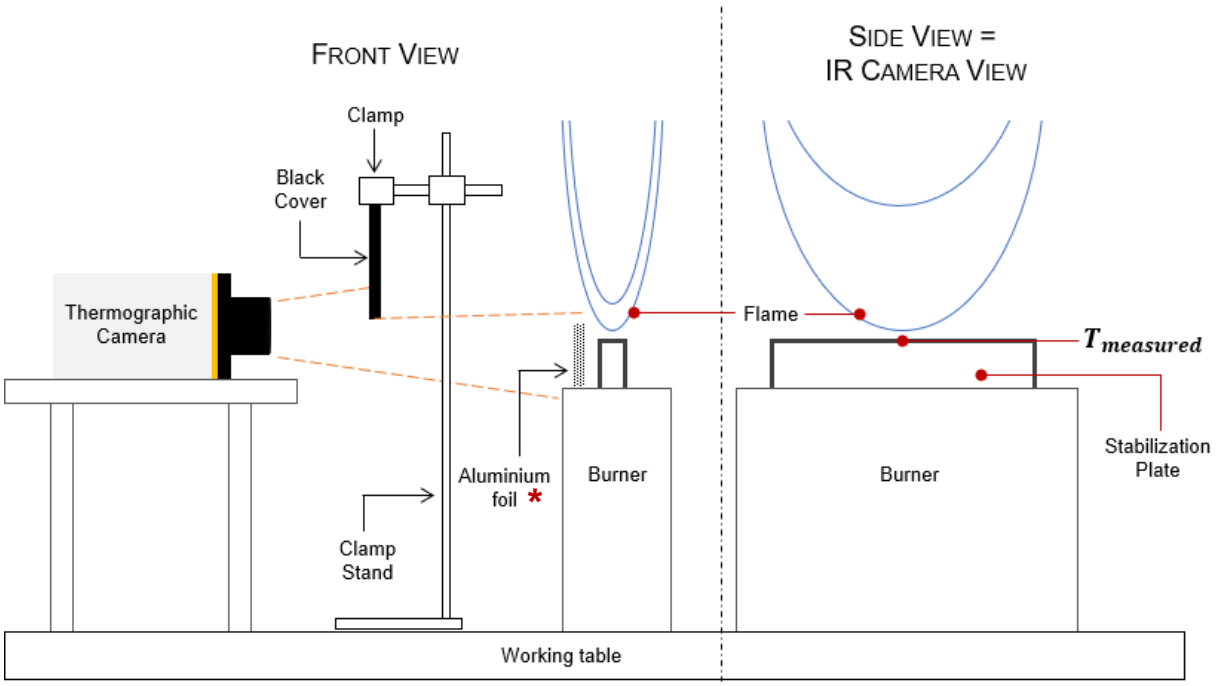

Figure 6 – Schematic diagram of the experimental setup used to perform the temperature measurements: (a) front view, showing where IR camera was placed, the flame radiation cover and the location of the aluminium foil used to evaluate the Tamb (b) side of the burner that is captured by the IR camera, indicating where the temperature measurement is performed. An original side view of the flame is also presented.
***** Aluminium foil was only used throughout Tamb quantification and not during surface temperature measurements.

Figure 7 exhibits the IR camera used and also a view of the temperature measurements in real laboratory conditions.

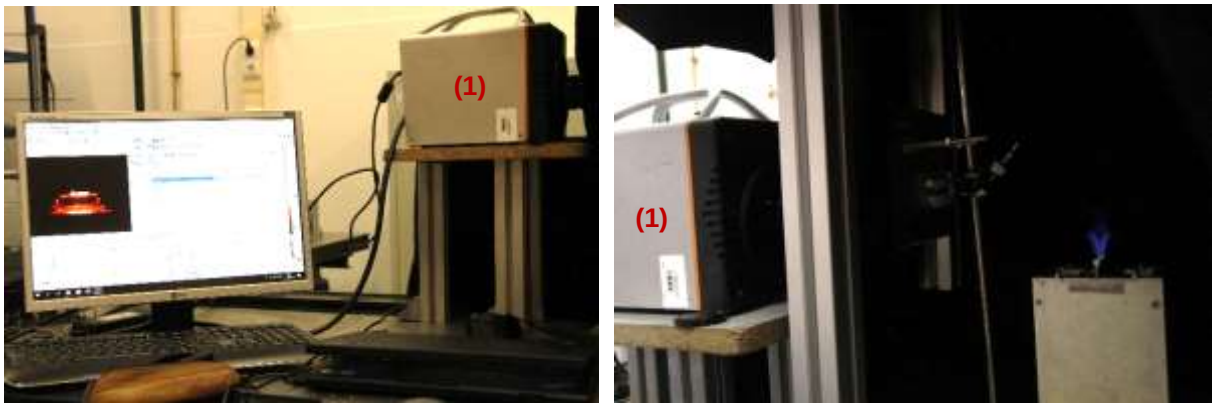

Figure 7 – Temperature measurements performed in laboratory: (a) data acquisition view and (b) burner side view. The number (1) corresponds to the IR camera used.

2.2.1 PROCEDURE FOR TEMPERATURE MEASUREMENTS

The temperatures measured correspond to a single point/pixel in the top edge of the plate, as illustrated in Figure 8. The camera was facing the lateral side of the flame holder and positioned in a stable and safe location close to the burner.

It was needed to use a black surface to cover up the flame and avoid flame radiation to the lens. With this strategy, it was possible to distinguish the flame base from the plate, allowing to choose the same pixel position along the various experiments using the camera's software.

Moreover, it is important to note that the measured temperatures don't correspond exactly to the centre of the end face where the flame is anchored. Nevertheless, due the small plate thickness (t=3mm) it was assumed that the plate behaves as an extended surface with a linear temperature distribution along the thickness.

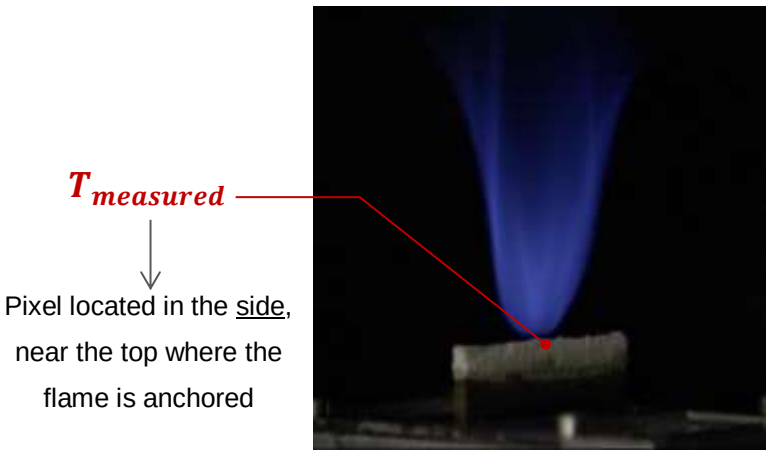

Figure 8 – Location where the temperature values were measured.

2.2.2 IR CAMERA INPUTS FOR TEMPERATURE MEASUREMENTS

Not all radiation acquired by this type of equipment is emitted by the target object. The participating media and the surroundings reflections are also parameters that should be considered, since any body with a temperature above 0K emits radiation. Consequently, when measuring the target object's temperature with the IR camera, there are other radiations sources that should be accounted. These sources are: the radiation emitted by the target object, the radiation emitted by the atmosphere and the radiation from the surroundings reflected by the object. Equation (3) represents the sum of all these elements:

$$W_{Total} = W_{obj} + W_{atm} + W_{refl} \tag{3}$$

in which W_{Total} corresponds to the total energy transmitted through radiation that is received by the IR camera. The suffixes *obj*, *atm* and *refl* refer to the radiation emitted by the object of study, atmosphere and radiation from the surroundings reflected by the objects, respectively.

Equation (4) derives from Equation (3) and express the variables that might influence the temperature measured of the object of study (T_{obj}),

$$T_{obj} = \sqrt[4]{\frac{W_{Tot} - (1-\varepsilon_{obj}).\tau_{atm}.\sigma_{SB}.(T_{refl})^4 - (1-\tau_{amb}).\sigma_{SB}.(T_{atm})^4}{\varepsilon_{obj}.\tau_{atm}.\sigma_{SB}}} \tag{4}$$

where, W_{Tot} is the total power (read by the camera), ε_{obj} is the object emissivity related to the material or coating characteristics of the object, T_{refl} is the surrounding equivalent reflected temperature, τ_{amb} is the transmittance of the atmosphere correlated to the distance of the object to the focal lens, T_{atm} the temperature of the atmosphere and σ_{SB} represents the Stefan-Boltzmann constant.

Figure 9 identifies the radiation sources represented in Equation (4).

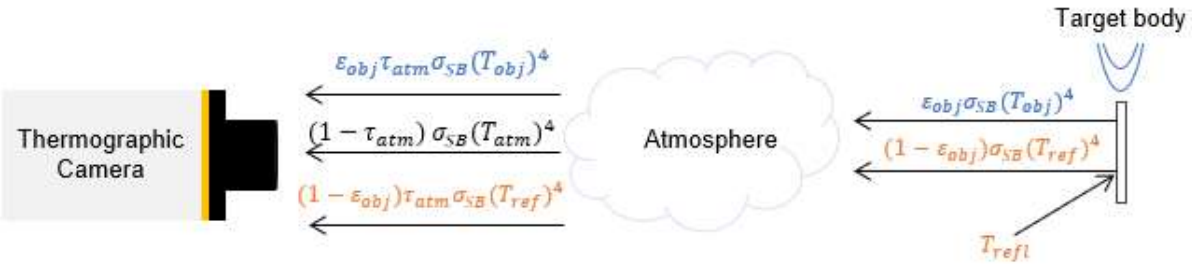

Figure 9 – Radiation sources received by the IR camera. Adapted from [23].

To measure and quantify the parameters related to the transmission and reflection through the surrounding air, the IR camera has two inputs: the atmosphere temperature (T_{atm}) and the ambient temperature (T_{amb}). The atmosphere temperature is evaluated by the equipment. This has one type-K thermocouple incorporated which is used to compute air transmittance by the camera's own software.

Regarding to T_{amb}, this value was estimated by placing a reflective object (e.g. sheet of aluminium foil) at the same distance from the camera as the target object. It has not possible to place the aluminium foil exactly at the level of the stabilization plate, as this would perturbate the flow. However, the obtained values are consistent and reliable as it is observed a decreased of T_{amb} values with decrease of ϕ. Furthermore, the operating range to evaluate T_{amb} was -120-135˚C. Notice that throughout the surface temperature measurements the aluminium foil was not used. The sheet of aluminium foil present in Figure 6 is exclusive for T_{amb} measurements.

Concerning to the SS plate emissivity, the values from Incropera et al. [24] were used, which offer a work range between 27˚C and 328˚C ($\bar{\varepsilon}_{AISI316} \approx 0.18$). To estimate the emissivity of the synthesized ZnO materials it was performed a study as it will be described next.

2.3 EMISSIVITY ANALYSIS OF SYNTHESIZED ZNO POROUS MATERIALS

An Ohmic heating (O.H.) was performed to estimate the emissivity of ZnO porous materials, as shown in the scheme of the Figure 10**.** O.H. is a process where heating of the materials is achieved by passing an electric resistance through it. In this experiment, an electric resistance with 500 Ω connected to a power supply, Huan Hsin SRV-10 Slide Voltage Regulator, was used to control the temperature on the stabilization plate (with ZnO materials deposited). Furthermore, half of the plate with deposited ZnO material was coloured using a black spray paint, which was used for reference. The black surface was assumed to have an emissivity of ε_{paint} ≈0.95-1 in camera input parameters.

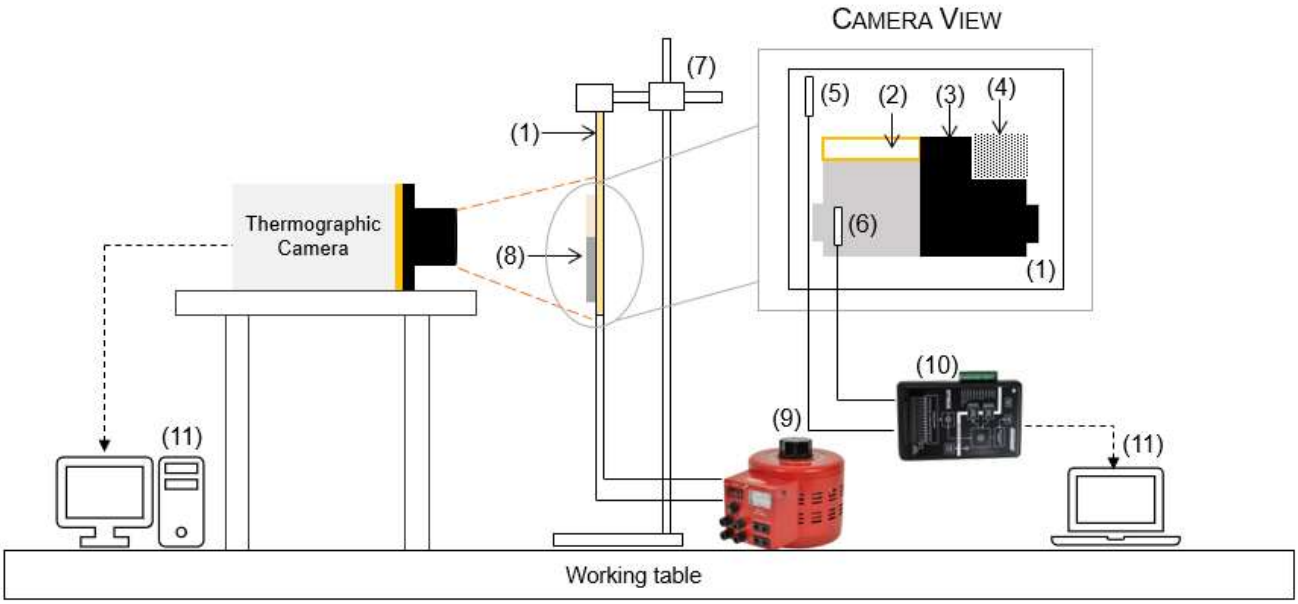

Figure 10 – Schematic view of experimental setup to estimate ZnO porous materials emissivity. It is present on the right side what is record by the IR camera: (1) electric resistance - 500Ω, (2) ZnO porous materials, (3) black paint, (4) aluminium foil (5) K-type thermocouple (placed in the electric resistance), (6) T-type thermocouple (placed in stabilization plate), (7) clamp stand, (8) plate with ZnO porous materials, (9) power supply, (10) Data Translation's DT9828 and (11) data acquisition.

As mentioned in previous section, the IR camera requires two inputs from the user: T_{amb} and the object emissivity. Therefore, it was placed an aluminium foil (represented in Figure 10 as number (4)) to evaluate the T_{amb}. Regarding the emissivity, since the ZnO material emissivity (ε_{ZnO}) is unknown, this value was measured by trial and error by taking as reference the temperature emitted by a black surface.

Additionally, two thermocouples were used in order to evaluate if the IR temperatures were in the same order of magnitude of those measured by the thermocouples. Figure 12 shows an orange curve which confirms the linear trend and identical magnitudes between the temperatures measured by the IR camera and by the thermocouple placed in the stabilization plate (number (6) in Figure 10) with a O.H..

The procedure applied to achieve a valid ε_{ZnO} was:

(i) Increase the temperature on the materials applying current through the electric resistance;

(ii) Achieve a stagnation temperature in the thermocouple placed in the electric resistance, presented in Figure 10 as number (5) ($time_{stagnation} \approx 20min$);

(iii) Record data using the IR camera defining three pixels (A, B and C, as shown in Figure 11 where, A is in the ZnO porous materials, B is in the black surface and C is measuring the T_{amb});

(iv) Define a T_{amb} input to the thermographic camera using pixel C ($\varepsilon = 1$);

(v) Measure T_B since it has a known emissivity (pixel B ⇒ ε_{paint} ≈0.95-1);

(vi) Manipulate $\varepsilon_A = \varepsilon_{ZnO}$ of point A until $T_A \approx T_B$ (trial and error method).

This procedure was performed between 20-180Volts with increments of 20V, resulting in a total of nine points. The values obtained for ε_{ZnO} are shown in Figure 12. Also, in Figure 12, the blue coloured area corresponds to the range of temperatures found in literature for similar experiments (Sung et al. [25] and Shoshin and Goey [26]). It was considered the emissivity values measured above 40˚C, resulting in a mean emissivity value of ZnO porous materials of 0.68

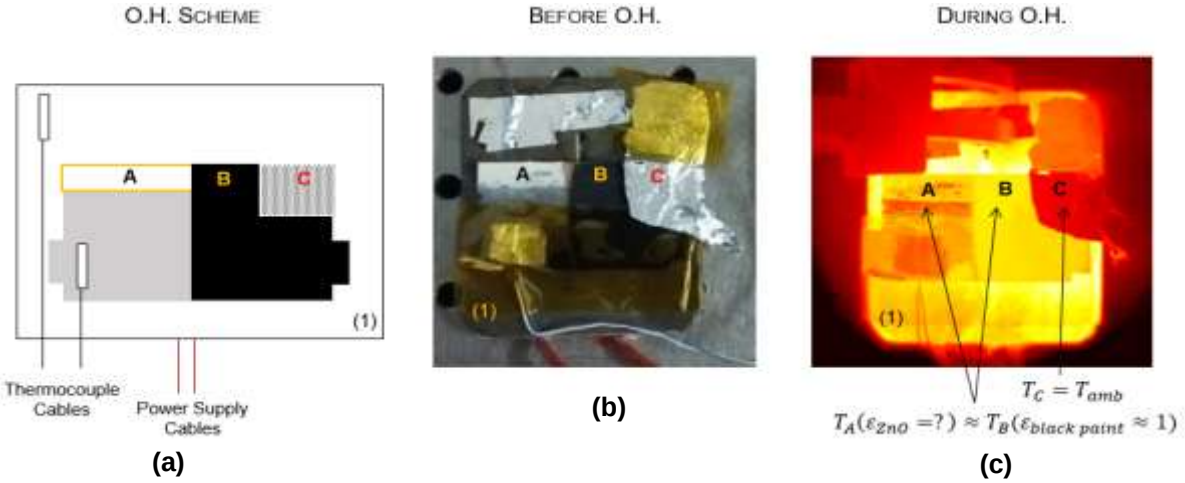

Figure 11 – (a) Scheme of O.H. setup used to evaluate the ZnO porous materials emissivity; (b) original set-up before the O.H. and (c) same as (b) but corresponding to the thermal image recorded by the IR camera. (1) is the electric resistance as shown previously in Figure 10. (A) is the ZnO porous materials, (B) black paint and (C) aluminium foil to T_{amb} measure.

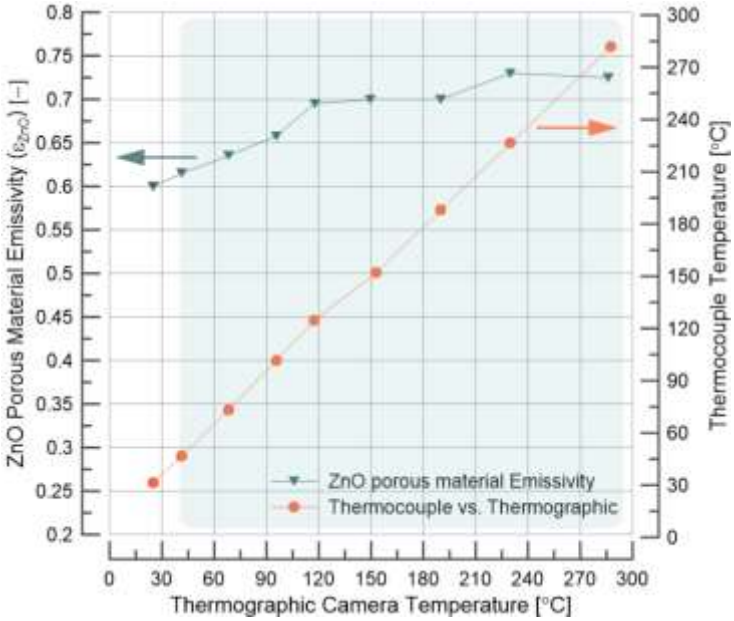

Figure 12 – Measured temperatures by thermographic camera vs thermocouple (orange curve) and obtained values for ZnO porous materials emissivity during the experiment.

2.4 STAND-OFF DISTANCES MEASUREMENTS

Canon EOS 7D was used to inspect the flames' behaviour, namely the flame profile as shown schematically in Figure 4 and in Figure 13(a). A manual focus was used, with an ISO of 1000 and a shutter of 1/10 in all photos. The main objective was to capture the instant before the flame blow-off, in particular to capture the flame shape and stand-off distance from the flame holder. All tests started with a fixed flow velocity (e.g. Re=100) and a ϕ=0.7. The parameter ϕ was then reduced in intervals of 0.01 allowing the flame to stabilized in the new condition (about *t*=15s). The decrements were performed until the flame extinguished, representing the photos the moment before the blow-off limit with $\phi_{images} = \phi_{blow-off} - 0.01$. This process was repeated several times for each flow velocity (Re range 100-700), to check against reproducibility of results. Figure 13(b) shows an example of an image taken just before the blow-off.

Figure 15 shows the steps used to analyse the stand-off distances through a MATLAB® routine, and Figure 14 exemplifies the approach used to define the scale of the images. Before processing the photos in MATLAB® the images were cropped using *ImageJ* to include the flame and the stabilization plate only, as shown Figure 15(b). The reference used to define the real position of the flame from the stabilization plate was a target with millimetric paper (Figure 14(a)). The scale of conversion from pixels to mm unity was performed using ImageJ, as illustrated in Figure 14(c). To evaluate the stand-off distance of the flame, a post procedure was carried out using a MATLAB® routine which are described follow (Figure 15).

(i) The colour channels (red, green and blue) are extracted from the original image

(ii) The pixel readings for the blue channel below the intensity level of 25 are identified from the image. Separation of this data avoids identifying the blue plume coming from the conversion of CO to CO_2. In this step, the flames base position is estimated and the criterion used to find the flames base in all images and experiments is defined;

(iii) The image is converted from RGB to a black and white format;

(iv) Two boundaries are defined: the flame base and the stabilization plate (red lines in Figure 15(c));

(v) The stand-off distance is calculated by subtracting the highest pixel from the boundary of the flame and the lowest pixel from the flame holder. This value is multiplied by the conversion factor already evaluated in Figure 14.

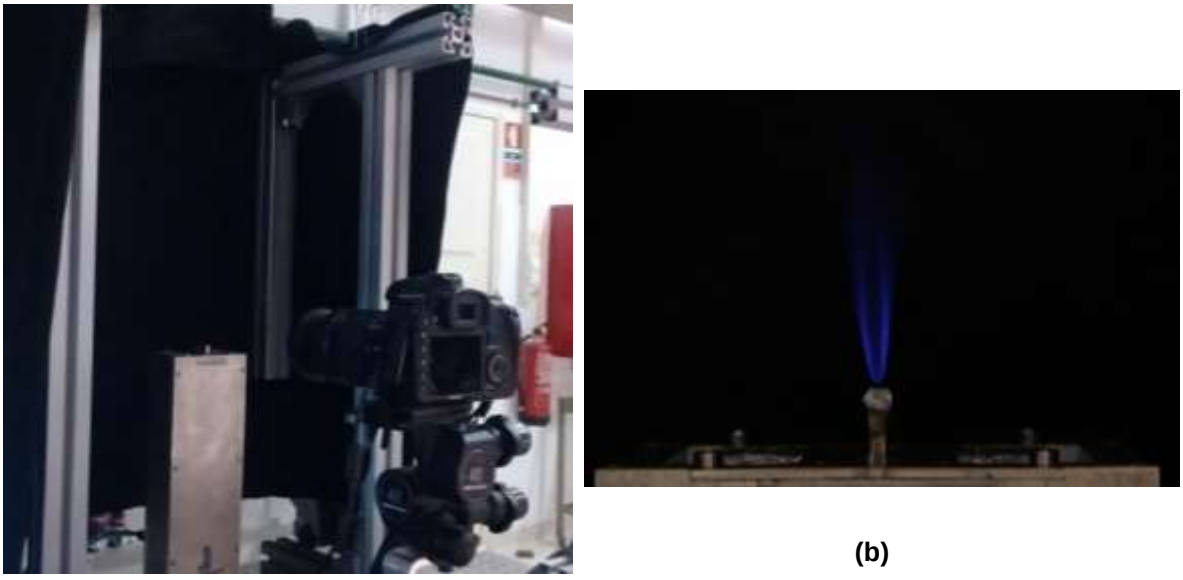

(a) (b)

Figure 13 – (a) Flame visualization set-up and (b) photo taken in the instant before the flame blow-off for a plate coated with ZnO porous materials (Re=300).

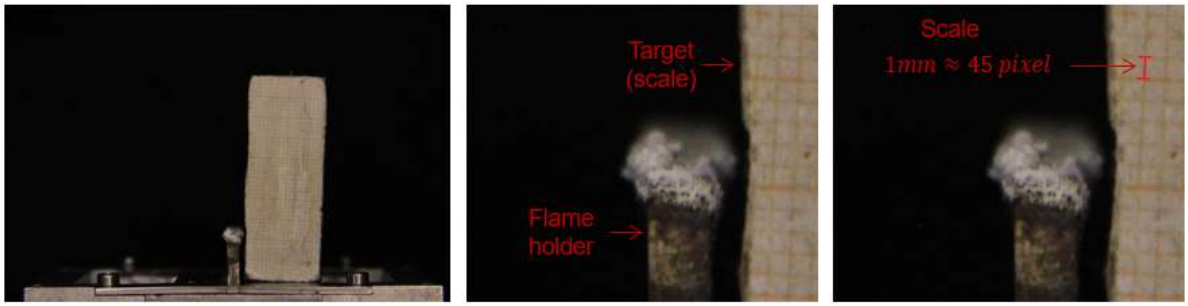

(a) (b) (c)

Figure 14 – Approach used to estimate the scale conversion to the stand-off distances: (a) photo taken before starting the tests using a target with a millimetric paper; (b) cropped illustration of (a) showing in detail the stabilization plate and the millimetric paper and (c) measurement obtained for 1mm using ImageJ (conversion factor=1/45).

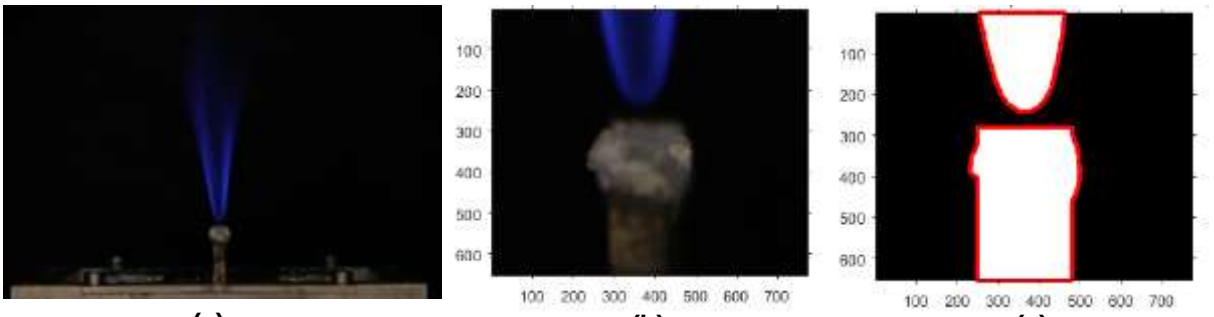

Figure 15 – Post processing adopted to evaluate the stand-off distances: (a) original photo of the instant previous to the flame blow-off in a plate with ZnO porous materials and Re=300. (b) Input image read by MATLAB® and (c) contour of the flame base and flame holder (red lines). The flame base was defined by counting only the pixels with an intensity level below 25 and the stand-off distance was defined as the shortest distance between the two contours.

2.5 ZnO Materials Preparation

The ZnO materials were electrodeposited onto both sides of a SS – the substrate was working as the cathode (Figure 2). Two types of electrolytes solutions (A and B) were used, differing each other only in the presence of the supporting electrolyte KCl as shown in Table 3. It was selected both solutions because it was intended to infer about the influence of KCl presence, since this element might promote material growth and also produce stronger structures Analytical grade chemicals and distilled water were used to prepare both solutions.

Table 3 – Electrolyte solutions composition.

Electrolyte	$ZnCl_2$ (Sigma-Aldrich)	NH_4Cl (Sigma-Aldrich)	KCl (Sigma-Aldrich)	pH (at T=20.5˚C)
A	0.5	0.5	2.0	4.88
B	0.5	2.0	-	4.35

The SS plates were previously polished with a 600 [P1200] grit paper (CarbiMet), ultrasonically cleaned in acetone for 3 minutes and dried with a jet of compressed air. All experiments were performed using an electrode cell connected to a power supply (Kikusui Electronics, Model PAB 32-3) at room temperature. During electrodeposition the SS plates maintained a constant active area of 5 cm^2, which was achieved using the same electrolyte solution volume (0.5 mL, reservoir dimensions, Figure 16(a)). Two plates of graphite were equally displaced (1.5 cm) from the SS plates used as anode. Electrodeposition was carried out in galvanostatic mode by applying a current density (i) of 0.1 to 0.4 A cm^{-2} for 60 and 90 s. The conditions were selected according to the maximum value of the power supply which is a current, *I*, of 2 A (i,e. *i*=0,4 A.cm^{-2}). Also, the *i* increments were chosen randomly in order to assess the different *i* values until the maximum value, and the time was also select arbitrarily. After experiments, all depositions were rinsed with ethanol and taken into an oven at 500˚C for 5 hours, for a thermal oxidation. In Table 4 is shown all produced samples according to different parameters and in Figure 16(b) is presented a ZnO materials deposited after the thermal treatment.

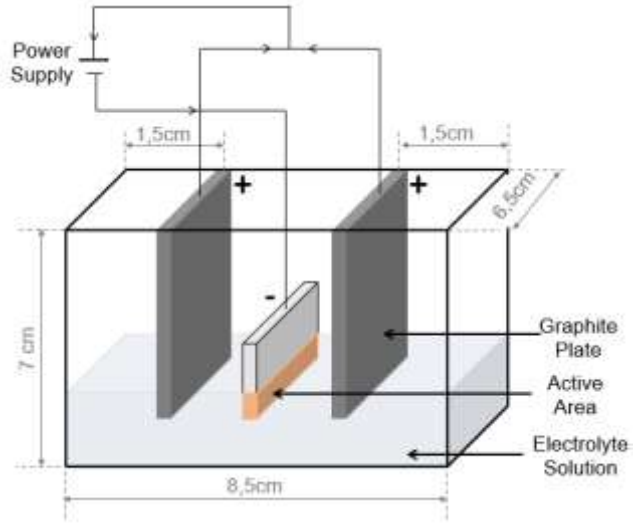

(a)

(b)

Figure 16 – (a) Electrodeposition set-up showing the active area where the material deposition occurs; (b) example of produced ZnO materials after thermal treatment.

Table 4 – Synthesized samples names and conditions.

Electrolyte A/B		
Time= 60s	*i* [A cm^{-2}]	Time= 90s
Sample		Sample
1	0.1	5
2	0.2	6
3	0.3	7
4	0.4	8

2.6 PHYSICO-CHEMICAL CHARACTERIZATION OF ZNO MATERIALS

Prior to combustion, structural analysis was performed using X-ray diffractometry (XRD) measurements at room temperature using Cu Kα radiation source (λ = 0.150619 nm) in a Bruker AXS-8 advance diffractometer with a Bragg-Brentano configuration (Figure 17(a)).

The motivation to use XRD is that it allows identification of the crystal structure of synthesised material, given that each material has its single pattern. Consequently, this technique allows the identification of the Zinc Oxide type in the produced samples and compare it against the X-ray spectrums with mineral species database found in literature, e.g as the RRUFF database [27,28]. The X-ray spectra from ZnO materials were collected over a 2Θ range from 10˚ to 70˚.

The morphology of ZnO materials before and after combustion experiments was characterized by scanning electron microscopy (SEM, Hitachi S2400). Also, the chemical composition analysis was done by the corresponding energy dispersive X-ray spectrometer (EDS), presented in Figure 17(b).

(a) (b)

Figure 17 – Equipment used to perform the ZnO morphologies characterization: (a) XRD diffractometer [29] and (b) SEM and EDS equipment [30].

2.7 AVERAGE PORES DIMENSION MEASUREMENTS PROCEDURE

Figure 18 shows the sequence of SEM micrographs post processing carried out to estimate the mean pores dimension of the porous materials tested on the burner. It was used an algorithm developed in MATLAB® R2017b software, applying features from the image processing toolbox as the Euclidean distance transform and the watershed transform (Gonzalez and Woods [31]). This analysis can be divided in two main topics: segmentation and histogram plotting. The approach used for segmentation was performed similarly to Eddins [32]:

(i) Conversion of a grayscale image (8bit) to a binary image as shown in Figure 18(a) and Figure 18(b), respectively;

(ii) Reduce image noise using a Gaussian blur;

(iii) Apply a Euclidean distance transform in order to find and recognise pores;

(iv) Optimize distance transform by imposing minimal area where neighbour pixels have a constant intensity. This step helps define the pores centre while minimizing overlap issues in the next step (watershed transform);

(v) Apply watershed transform which allows to differentiate higher and lower regions with bright and dark contrasts;

(vi) Image is now segmented and ready to analyse pores distribution. This final treated image is presented in Figure 18(c).

Finally, the density distributions were computed using also MATLAB®.

The developed routine is presented in Appendix A.

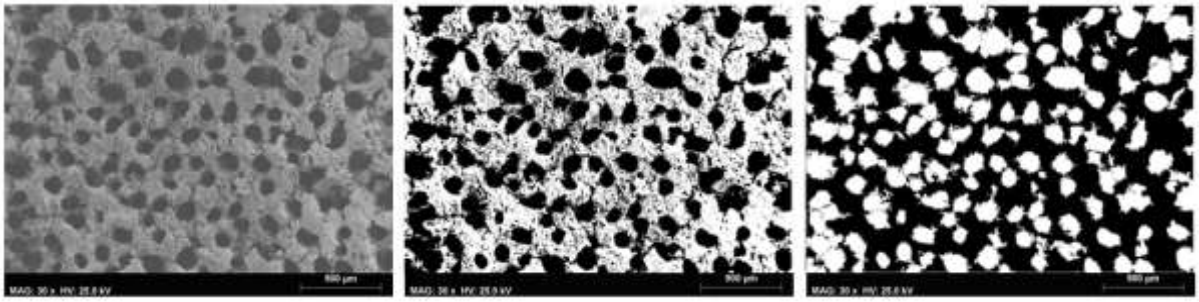

(a) **(b)** **(c)**

Figure 18 – Procedure used to evaluate pores dimension: (a) original image (input in MATLAB® routine); (b) binary image, i.e., normalized image intensity to values between zero ("black") and one ("white") and (c) result image after applying the Euclidean distance transform and watershed transform in MATLAB®. This latter image is already segmented.

2.8 UNCERTAINTY ANALYSIS

This topic addresses the uncertainties associated with the collected experimental results. All the results obtained are subject to several systematic errors and statistical fluctuations. The latter error appears due to the precision limitations of the measurement device equipment. To minimize this type of error all experiments were performed multiple times in order to check against reproducibility and accuracy.

2.8.1 FLOW CONTROLLERS

The flow meters, shown in Figure 4 and Figure 5, used throughout the experiments have uncertainties associated with the flow rate output. The total uncertainty for a determined flow rate (ξ_Q), is given by the sum of the error related with reading (0.8%) and scale (0.2%), as expressed by Equation (5),

$$\xi_Q = \pm(0.008Q_m + 0.002Q_{max}) \quad (5)$$

Where, ξ_Q is the uncertainty of the flow rate Q, Q_m represents the measured flow rate and Q_{max} is the maximum operating flow rate allowed by the flow controller (CH_4 or air). A relative error (e_Q) associated with the flow rate measured is possible to compute from ξ_Q. Table 5 exhibits the results obtained for the maximum uncertainty of both flow meters used.

Table 5 – Uncertainty and maximum relative error of each gas volumetric flow rate.

Gas	Highest Q_m [SLPM]	Q_{max} [SLPM]	ξ_Q [SLPM]	e_Q [%]
CH_4	2.88	5	± 0.3304	1.15
Air	26.55	50	± 0.3124	1.18
Total	29.43	55	± 0.3454	2.32

This uncertainty has an influence in the Re and ϕ recorded for each flame. Consequently, an error propagation must be considered to estimate the uncertainties of these latter parameters.

2.8.2 EQUIVALENCE RATIO

The Equation (2), which defines ϕ, can be rewritten as function of volumetric flow rates of methane and air, $Q_{CH_4}$and Q_{air}, respectively, as shown in Equation (6)

$$\phi = \frac{a\, Q_{CH_4}}{x_{O_2}^{air}\, Q_{air}} \tag{6}$$

where, a represents the stoichiometric coefficient of oxygen for complete CH_4 combustion, and $x_{O_2}^{air}$ is the average molecular fraction of oxygen present in atmospheric air at sea level. For CH_4, a=2 and $x_{O_2}^{air}$ assumes a value of 0.2095 [33]. Neglecting the uncertainty associated with the reactants densities, the equivalence ratio uncertainty, ξ_ϕ, might be expressed as follow

$$\xi_\phi = \pm \frac{2}{x_{O_2}^{air}\, Q_{air}} \sqrt{{\xi_{Q_{CH_4}}}^2 + \left(\frac{Q_{CH_4}}{Q_{air}}\right)^2 {\xi_{Q_{air}}}^2} \tag{7}$$

Taking the values present in Table 5 and the smallest Q_{air} obtained (3.81 SLPM for ϕ=0.57), the maximum uncertainty related to equivalence ratio can be estimated. The result obtained is listed in Table 6.

Table 6 – Maximum uncertainty and relative error related with equivalence ratio

$\xi_{Q_{CH4}}$ [SLPM]	ξ_{Qair} [SLPM]	ϕ [-]	ξ_ϕ [SLPM]	e_ϕ [%]
± 0.3304	± 0.3124	0.57	±0.0181	3.18

2.8.3 REYNOLDS NUMBER

An analogous approach of error propagation can be performed for Reynolds number. Equation (1) can be reformulated as function the total flow rate, $Q_{Total} = LA$, leading to Equation (8)

$$Re = \frac{L}{A\,\nu} Q_{Total} \tag{8}$$

Where, L is the burner length [m], A corresponds to the area of the channel [m^2], and ν is the mixture kinematic viscosity [m^2/s]. The uncertainty associated with Re, ξ_{Re}, and its relative error are presented in Table 7.

Table 7 – Maximum uncertainty and relative error related with Re

$\xi_{Q_{CH4}}$ [SLPM]	ξ_{Qair} [SLPM]	ξ_{QTotal} [SLPM]	Re [-]	ξ_{Re} [SLPM]	e_{Re} [%]
± 0.3325	± 0.3325	± 0.3454	700	± 10.3512	1,48

2.8.4 TEMPERATURE MEASUREMENTS

The thermographic cameras are designed and calibrated to operate in IR spectrum, which lies between visible light and microwaves [34]. However, an accuracy of a temperature measurement relies on key issues as already reported in section 2.2.2: reflections from surroundings objects and surface emissivity. Additionally, in IR spectrum the shape and boundaries of the target object aren't as easily to distinguished as in the visible region, which may also be an error source.

According to the IR camera manufacture (*Xenics*), they guarantee precision of ± 2 ˚C. This may be corroborated by the orange curve in Figure 12, in which the temperatures read by the camera and the thermocouple have a linear trend.

CHAPTER 3

RESULTS AND DISCUSSION

This chapter analyses and infer about the results collected during the experiments. It is divided into main groups. First part is dedicated to the samples synthesised (ZnO), presenting the electrodeposition conditions in which its possible to fabricate porous morphologies. Also, it is present the materials that were selected to perform the burner tests. The second group is a detailed analysis of the flame stability with ZnO porous materials acting as stabilization plate. A study of the heat flux that is involved in the stabilization mechanism is also performed in this latter group.

3.1 ZINC OXIDE MATERIALS

3.1.1 CHARACTERIZATION OF ZINC OXIDE MATERIALS

Figures 19(a) and 19(b) shows the X-ray diffractograms of ZnO materials -corresponding to the electrolyte A and B, respectively (Table 3). The peaks found in X-ray diffractograms are assigned to a phase which is a specific chemistry and atomic arrangement. Each phase produces a unique diffraction pattern [35]. Recall that electrolyte A corresponds to the aqueous solution with KCl in its composition.

The X-ray diffractograms of the ZnO materials showing diffraction peaks in the 2θ range 10^{o}–70^{o}, corresponds to the characteristic reflections of zincite (ZnO) (RRUFF ID: R050419) [28] structure. The two peaks identified with the red dashed lines in electrolyte A. Figure 19(a), can be assigned to KCl impurities, since these peaks found at 28.5˚ ad 40.8˚ agree with those found in RRUFF data base for sylvite, KCl (RRUFF ID: R050166) [27].

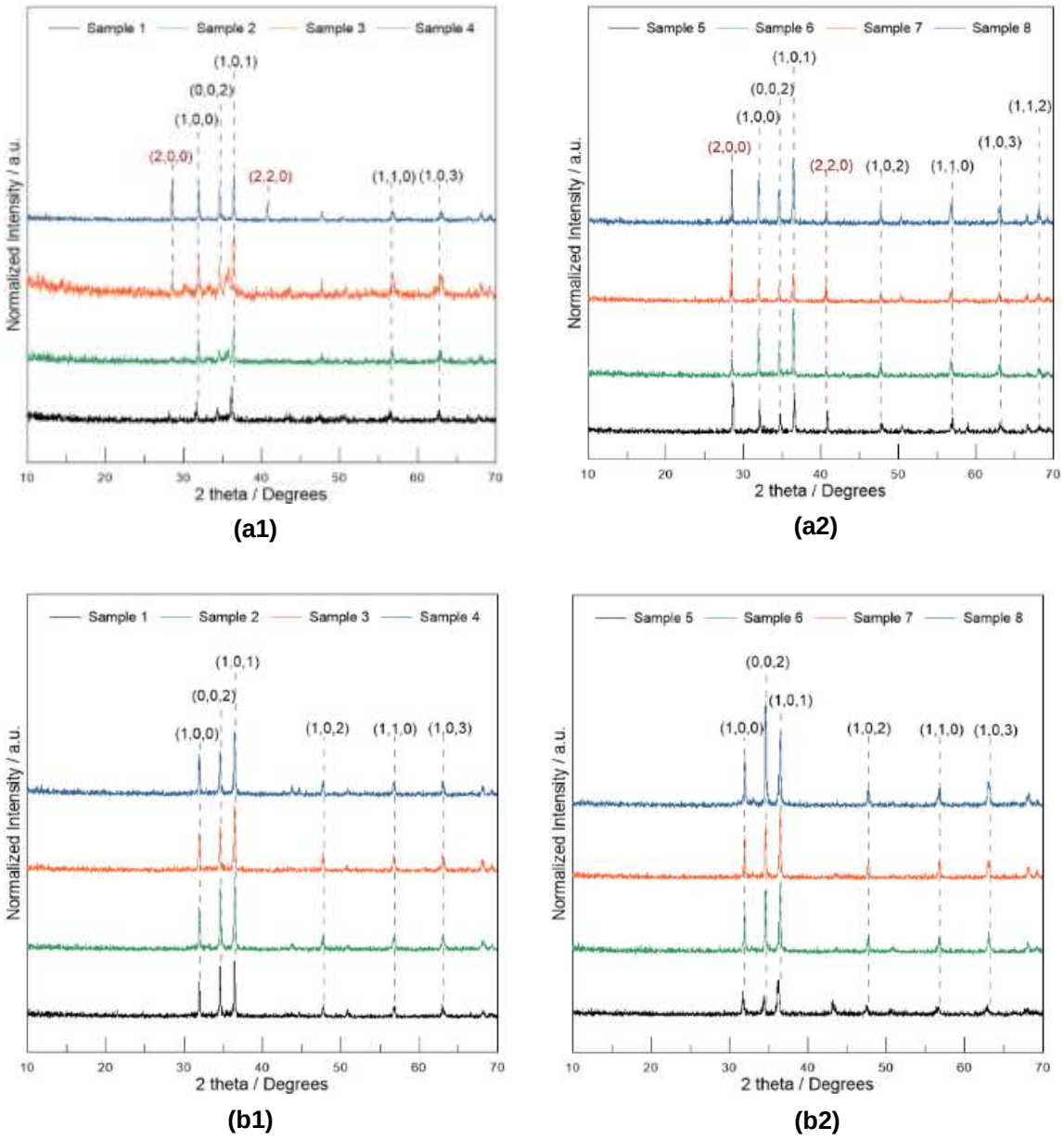

Figure 19 – X-ray diffractograms: (a1) electrolyte A (w/ KCl) and t=60s; (a2) electrolyte A and t=90s; (b1) electrolyte B (w/o KCl) and t=60s; (b2) electrolyte B and t=90s.

The SEM micrographs presented in Figure 20 show the evolution of the synthesized ZnO materials evidencing the formation of a porous structure under higher *i* (*i*>0.3 A.cm^{-2}) and longer deposition times (*t*), The six porous materials highlighted in Figure 20 with red lines were the ZnO materials selected to perform the flame stabilization tests, since are the samples that have a porous morphology.

Due to the DHBT method as explained earlier in the section 1, with higher *i* occurs an increase of the bubbles density originating pores with the same dimension as the diameter of the released bubbles [22]. A 3D structure with interconnected porosity was produced in both electrolytes (A and B) for the same electrodeposition conditions: *t*=60s+*i*=0.4 A cm^{-2} and *t*=90s+*i*=0.3 and 0.4 A cm^{-2}.

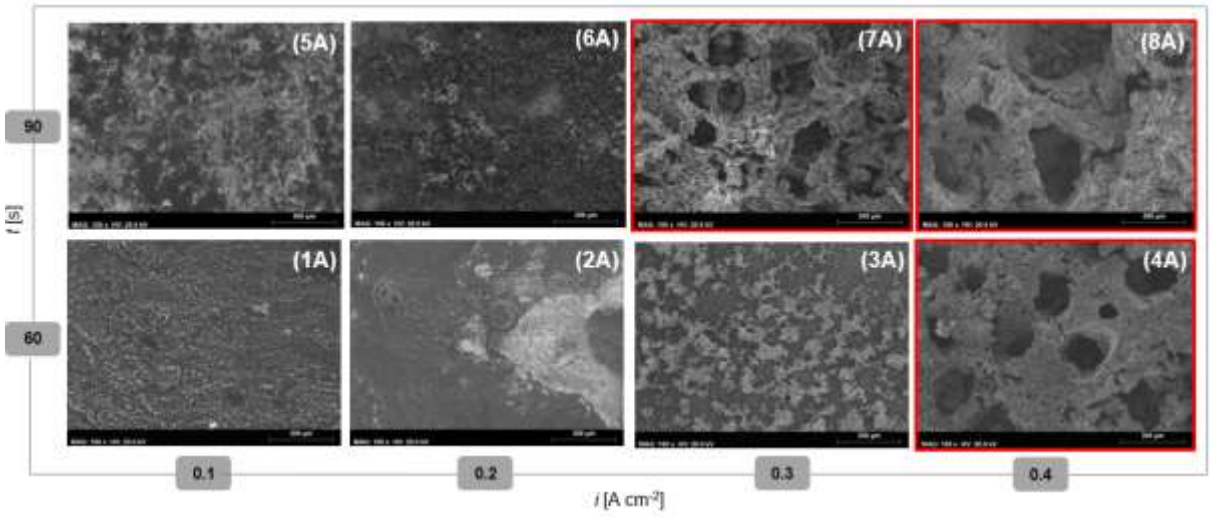

(a)

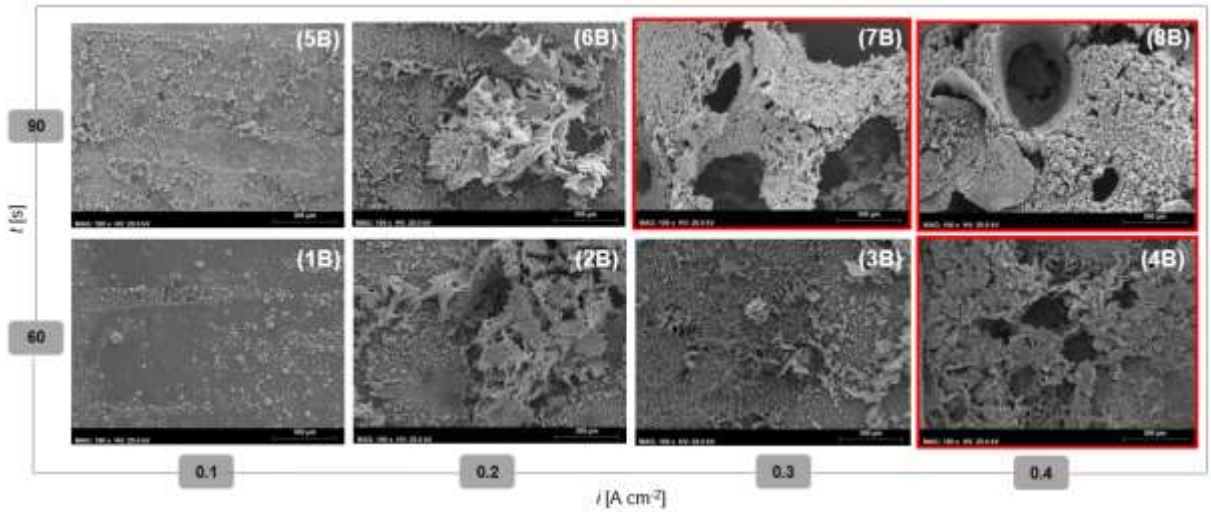

(b)

Figure 20 – SEM micrographs of synthesized samples according t and *i*; (a) electrolyte A; (b) electrolyte B (without KCl). The highlighted samples with red lines were the material selected to perform experiments in the burner since it shows a porous structure.

	Electrodeposition Conditions		
Electrolyte	*t*=60s *i*=0.4 A cm^{-2}	*t*=90s *i*=0.3 A cm^{-2}	*t*=90s *i*=0.4 A cm^{-2}
A [W/ KCl]	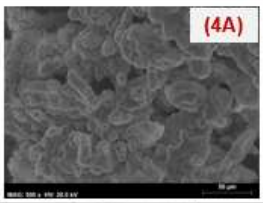	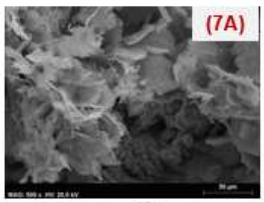	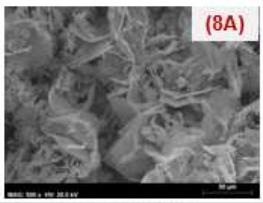
B [W/O KCl]	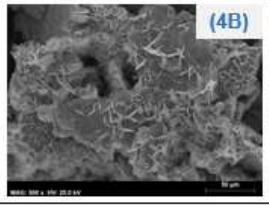	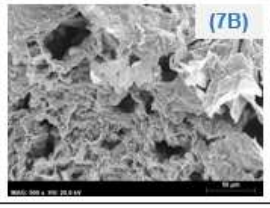	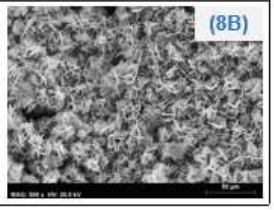

Figure 21 – Higher magnification (500x) of the selected porous materials (marked with red lines in Figure 20) to perform tests in the burner.

A higher magnification at the six ZnO materials selected with a porous surface – Figure 21 – shows a morphology composed by hexagonal-like subunits, which are a typical nanostructure in ZnO [19].

Since electrolyte A has in its composition KCl it was found KCl crystals in the samples produced by this electrolyte. Figure 22 shows a SEM micrograph of a KCl crystal (solid line) and the EDS performed in the two marked areas proving the presence of the crystals.

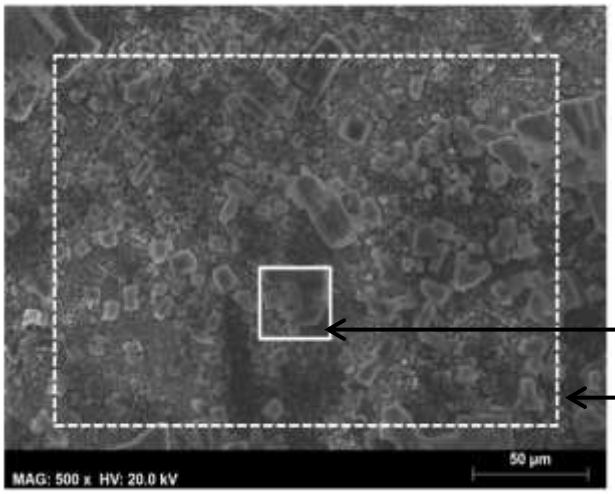

Chemical Element	Atomic Weight [%]	
	Solid line	Dashed line
Zn	30.2	81.3
O	10.8	1.0
Cl	20.0	3.0
K	29.0	2.7

Figure 22 – Evidence of formation of KCl crystals in produced samples with electrolyte A (w/ KCl). EDS was performed in the two mentioned areas, where the solid lines is a KCl crystal.

Figure 23 and Figure 24 present the chemical composition (at atomic weight %[1]) detected by EDS of all produces material. The chemical elements detected in the deposited material are Zinc (Zn), oxygen (O), potassium (K) and chlorine (Cl). Notice that the thermal treatment performed in the

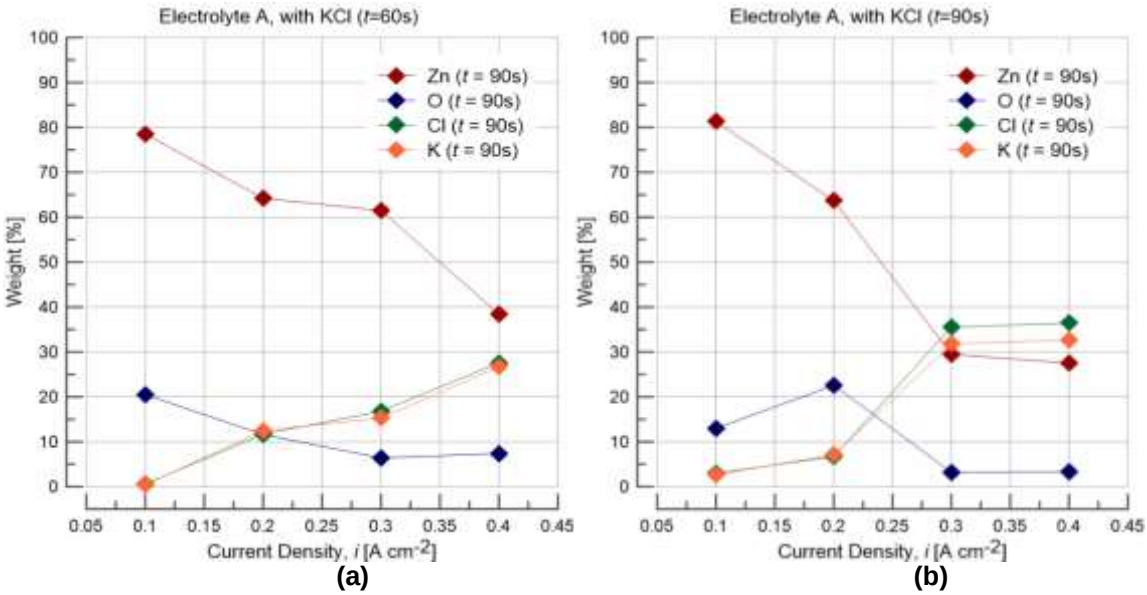

Figure 23 – Evolution of the chemical elements present in synthesized ZnO materials for electrolyte A (w/ KCl) for (a) 60s and (b) 90s electrodeposition times.

[1] Atomic weight refers to the mass of each element (in percentage) detected by the equipment.

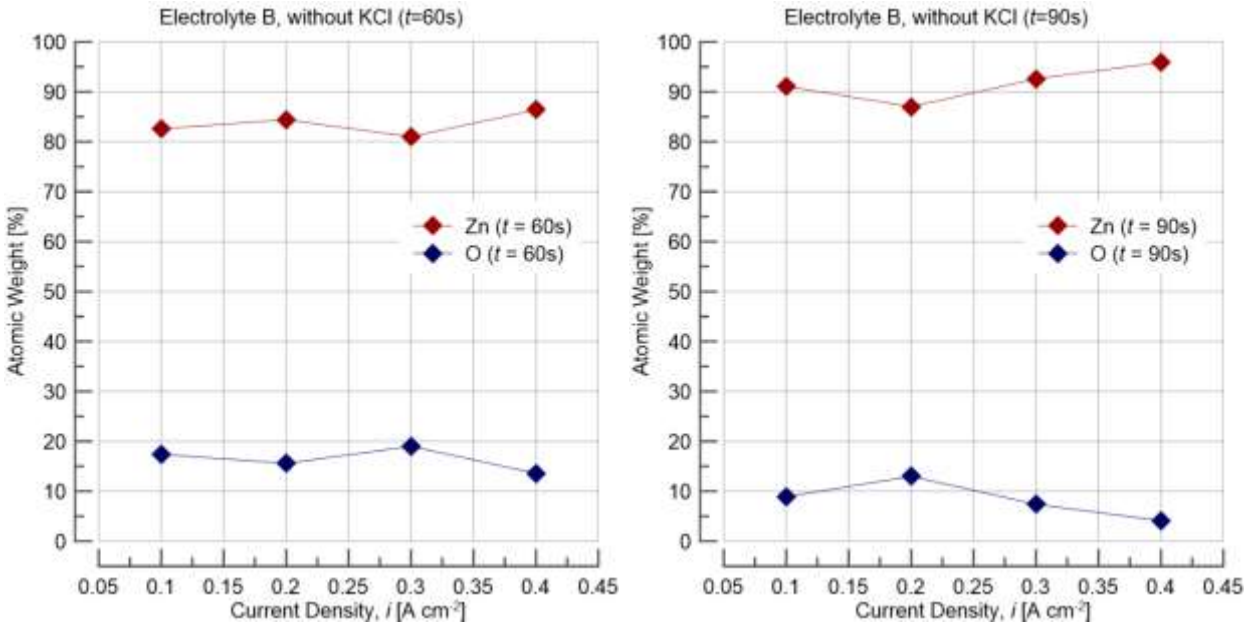

Figure 24 – Evolution of the chemical elements present in synthesized ZnO materials for electrolyte B (w/o KCl): (a) 60s and (b) 90s electrodeposition times.

electrodeposition procedure allows to transform Zn-derived materials in zinc oxide, since elements as chloride (Cl) and hydrogen (H) are eliminated

Regarding to EDS for electrolyte A (Figure 23), a decrease on Zn (red line) detection is observed and a parallel increase of Cl an K elements (green and orange lines, respectively) along increments of *i*. This is due to the formation of KCl crystals (Figure 22) which covers more surface and consequently leads to the reduced emission of Zn. It is evident an increase of K and Cl curves, which nearly overlap, evidencing the growth of KCl crystals.[2]

Regarding electrolyte B (Figure 24), EDS shows the same order of magnitude of the Zn element in the composition of all produced samples (between 80 and 95% in atomic weight), without showing any trend with the manipulated parameters (time and *i*) as seen with electrolyte A.

The small values of chemical element O in both electrolytes is because of its weight. Since O is light element with a poor vibration when excited, the equipment can't detect its emission.

The obtained results from XRD and SEM/EDS confirm the formation of ZnO as intended in all synthesized material. Also, longer electrodeposition times and higher i allowed to produce material with a 3D porosity structure with different pores dimension to use in the burner (marked in Figure 20).

3.1.2 DEPOSITED MASS THICKNESS

Figure 25 shows the thickness evolution of the obtained mass deposits. The thickness was estimated by SEM micrographs of the cross-section of the ZnO porous materials.

[2] Attention to the fact that the atomic weight values presented in Figure 22 for the dashed line are slightly different of the values shown in Figure 23(a). The EDS were performed in different areas of the sample, and consequently, the values might fluctuate according to the zones that are been analysed

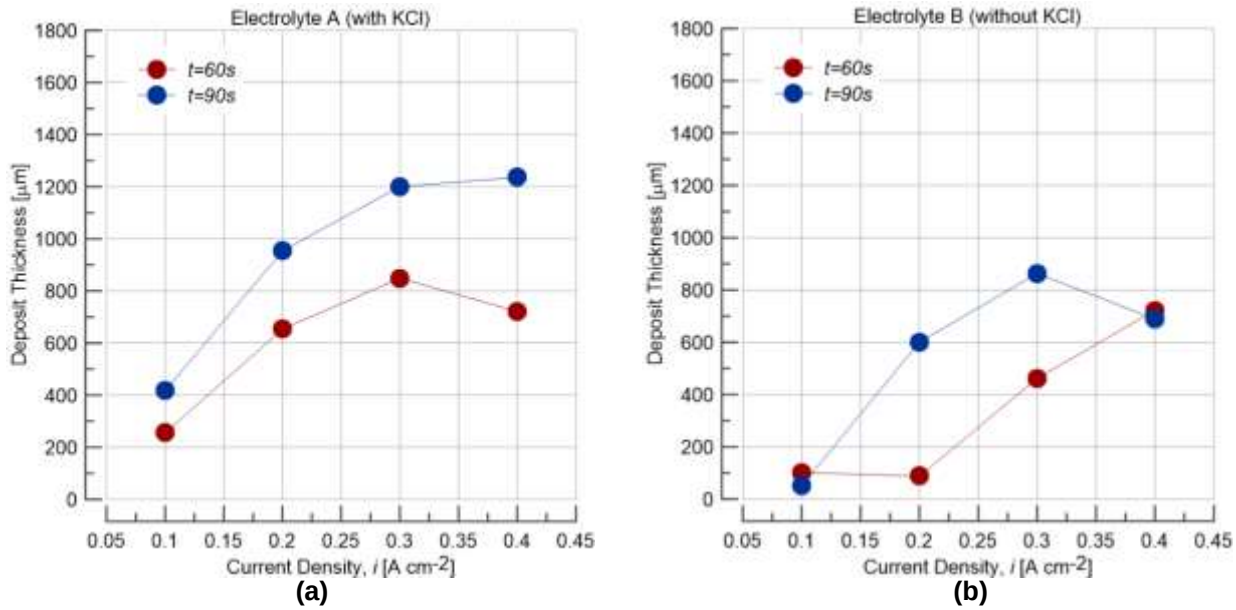

Figure 25 – Evolution of ZnO materials thickness with *i* (a) electrolyte A and (b) electrolyte B.

Once again, these results confirm the KCl role at mass growth since a thicker surface with equal conditions is achieved for electrolyte A. Also, the increase of *i* and electrodeposition times leads to thicker depositions. Nevertheless, observing samples with same deposition time but higher *i* (for instance, 7A and 8A) it's possible to conclude that the thickness decrease is owning to the bubble density. Higher *i* leads to an instability of larger bubbles [22] due the its residence time, in fact this leads to larger pores, however, the growth mechanism is not able to cope with the size increase.

3.1.3 AVERAGE PORES DIMENSION

Probability distribution of the dimensions of the porous materials used to perform combustions experiments (highlighted in Figure 20), are shown in Figure 26.

From Figure 6 it is possible to infer that electrolyte A provides a wider range of pores sizes when comparing with electrolyte B. Also, the porous materials produced with higher *i* have larger pores: for instance, D_m (7A) is smaller when comparing with D_m (8A), both having the same deposition time (90s) but different *i*. The measured D_m values are within the range reported in literature [20,36] for this type of surfaces.

The importance of KCl presence in electrolyte solution will be now be evaluated. For the same conditions (sample 4, for instances) KCl provides a bigger pores formation due to the accelerate growth mechanism [20,36]. The porosity (without KCl) for high current densities is slightly higher, despite having a similar order of magnitude as found for solutions with KCl in composition. This result suggests that the absence of KCl leads to pores walls with a lower density, and, consequently, a slight increase in the porous diameters.

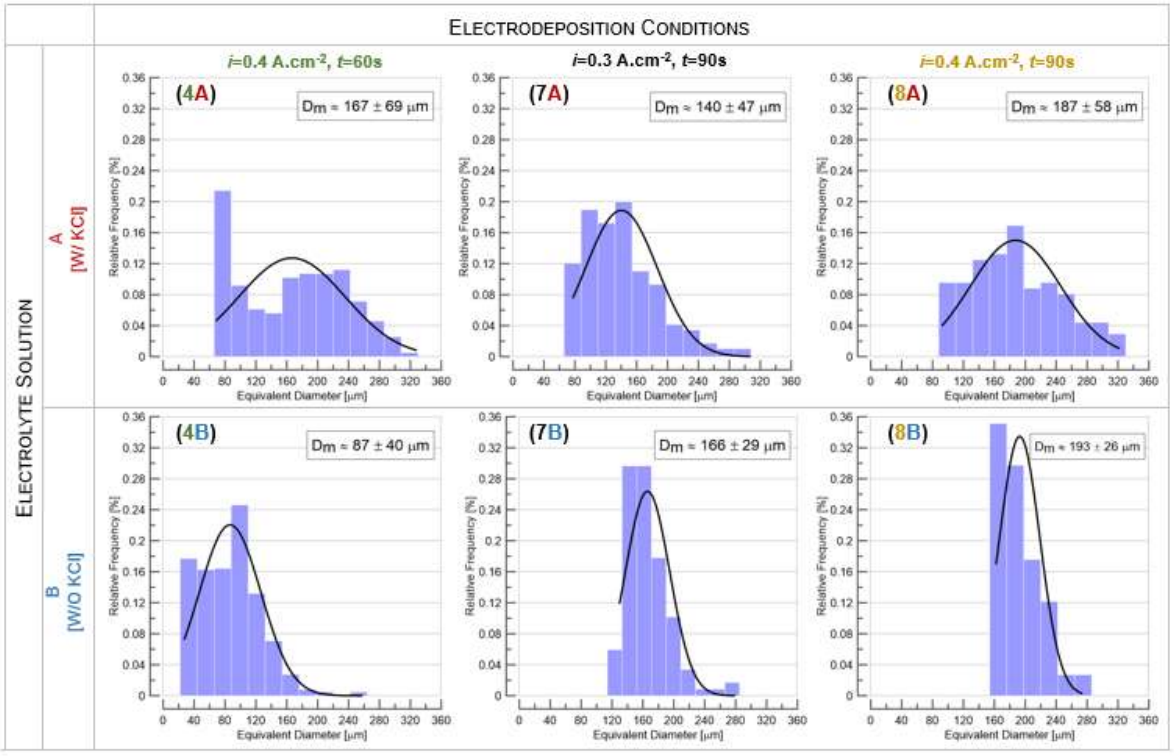

Figure 26 – Pores size distribution with respective mean diameter (D_m + standard error).

3.1.4 ZnO Porous Materials: Before and After Combustion Experiments

Table 8 and Figure 27 shows the EDS and SEM micrographs of ZnO porous materials before and after performing combustion experiments with the burner, respectively.

Table 8 – Chemical composition (at wt%) of the elements detected by EDS after combustion tests.

	Atomic Weight [%]					
Chemical Element	4A	7A	8A	4B	7B	8B
Zn	46.7	39.5	46.7	89.7	86.5	85.9
O	8.0	22.8	18.1	10.7	13.5	14.1
Cl	22.3	18.9	19.8	-	-	-
K	23.1	18.8	15.4	-	-	-

Comparing the before and after images of the porous samples in Figure 27 it can be seen that only electrolyte A remained the porous structure. It is believed that the presence of KCl in solution A may influence the formation of intrinsic defects by changing the morphology of the deposited material as demonstrated by Tena-Zaera et al [37], leading to the synthesis of a firmer surface. Electrolyte B loses completely its porosity structure, leading to a poor and delicate material, and making it unsuitable

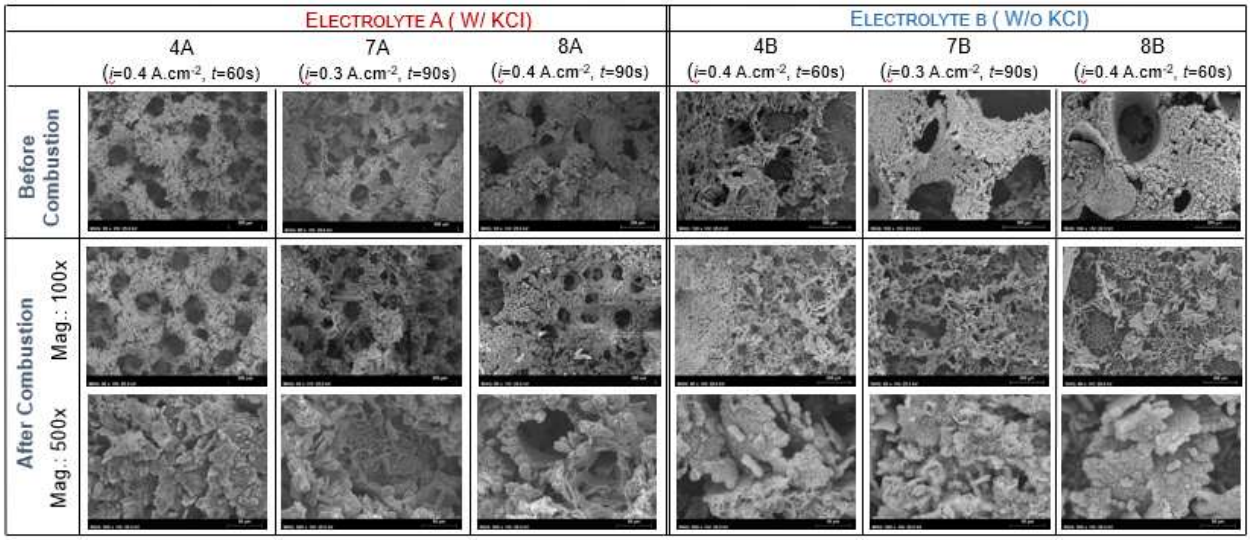

Figure 27 – SEM micrographs obtained before and after burner' experiments of ZnO porous materials. The bottom images are a higher magnification (500x) of the micrographs with 100x magnification.

for this type of application. However, besides the produced material are being delicate and needed to be handled with care, visually there is no degradation of the material.

Considering the chemical composition after combustion, it has been observed a decrease of Cl and K elements in the electrolyte A. The adiabatic flame temperature (Tad) is always higher than the KCl melting point (770˚C) found on PubChem database [38], even with lean equivalence ratios, which can justify the decrease detection of these elements. The KCl crystals observed in Section 3.1.1 –Figure 22 – doesn't appear in SEM micrographs, corroborating once again the reduction K and Cl detection in EDS. Regarding to Zn and O elements remain in the same order of magnitude as measured in previous combustion experiments (Figure 23 and Figure 24).

3.2 COMBUSTION

The criterion behind the stabilization of inverted flames isn't consensual in scientific community, since there isn't a clear understating about the phenomena's that are controlling the flame stability. Lewis and Von Elbe [11] and Edmondson and Heap [12] support that it is the positive stretch of the base flame leads to a higher heat loss to the unburnt mixture, and consequently occurs a local flame extinguishment. In another hand, Sung and Law [25] show in their investigations that contributions from both flame stretch and flow straining are important for the flame stabilization. Additionally, Trevino et al [39] claim that it is the heat transfer between the stabilization plate and the flame is essential for stabilization. Summarizing, the flame curvature, flow straining due to the flame presence, simultaneous mass and heat transfer are effects that justify the flame stabilization.

Although the unclear justification of the stabilization mechanism, it was carried out a study about the heat flux that it is involved the flame blow-off, in order to understand the stability diagrams obtained and infer about the porous surface as a flame holder.

3.2. LEAN STABILITY DIAGRAMS

The flame stability criterion was defined as the blow-off moment, since before achieving this limit the flame is a well-defined and stable V-shape. As explained in Stand-Off Distances Measurements section (Section 2.4), for each flame holder the tests started with a fixed flow velocity (e.g. Re 100) and ϕ=0.7, decreasing ϕ in intervals of 0.01 and allowing the flame to stabilize. Once the flame extinguished, the conditions of this blow-off moment were recorded in the flowmeter's software (element (4) in Figure 4). Each condition was performed several times in order to check against reproducibility. The blow-off data provided by the flowmeter's software allowed to obtain stability diagrams.

Figure 28 shows the stability limits obtained for all the six-porous ZnO materials tested. The black square data points refer to a clean stabilization plate without material deposited (SS plate) and is used as a reference measurement. The values measured for the reference holder are in the same order of magnitude with those found in literature [10]. For low flow velocities it can been seen that all porous materials have an opposite effect on the flame stabilization, since the blow-off occurs at higher ϕ which is not a desirable behaviour. However, the porous material tends to have the same action as the clean surface with an increase of mixture velocity, allowing an approximation of all stability curves to the reference curve. Notice that for electrolyte A (Figure 28(a)) the ZnO material with smaller pores (green curve, Dm ≈ 140μm), when compared with the other produced materials with bigger pores, has a similar trend as the reference curve (black line). This also applies to sample 4A (Dm ≈ 167μm) given the stability line also approaches the reference curve.

In addition, it is visible a higher displacement of the electrolyte B curves (Figure 28 (b)) comparing with electrolyte A (Figure 28 (a)) from the reference curve. This is due to the ZnO porous material produced with electrolyte B losing completely their morphology as shown in after combustion SEM micrographs (Figure 27). The deposited mass led to a difficulty in flame stabilization. This result verifies the importance of KCl role in the process, since its presence allowed to preserve the flame at lower ϕ.

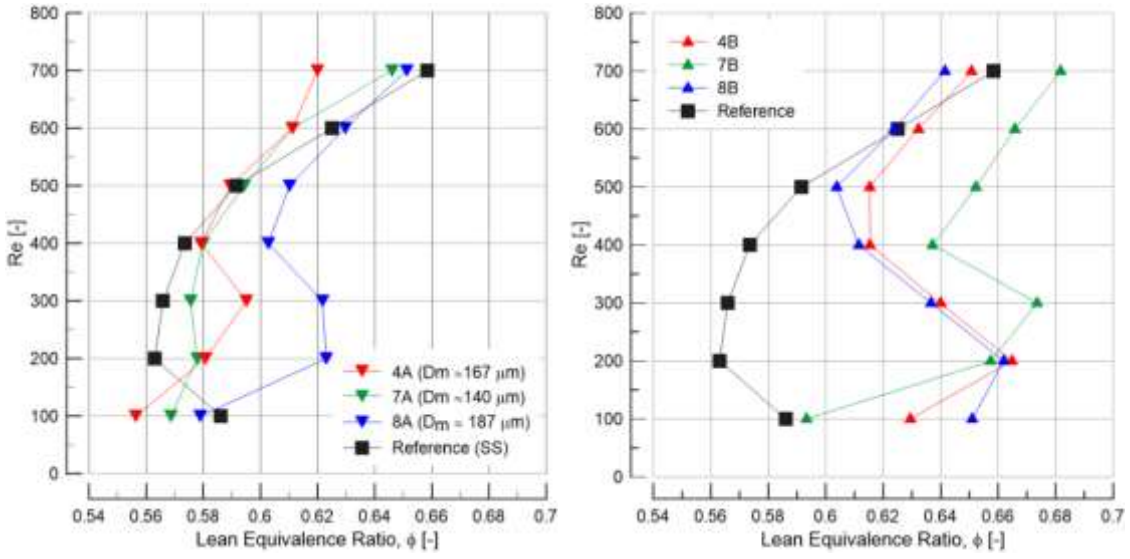

Figure 28 – Lean stability diagrams: (a) electrolyte A (w/ KCl) and (b) electrolyte B (w/o KCl). D_m stands for the mean diameter of the synthesized porous material. In electrolyte B the D_m values were omitted since its materials lose completely their porous morphology after performing the combustion tests.

3.2.2 TEMPERATURE

The ϕ decrease is accompanied by a parallel decrease of the adiabatic flame temperature (T_{ad}), since it will vary the fuel-air composition and consequently, change the chemical composition of the combustion products. Also, lower ϕ implies that part of the reaction energy that is released is used to heat the excess air, leading to a decrease of T_{ad} [40]. However, not only the Tad is influencing the temperature on the stabilization plate. The flow velocity and gap between the base flame and the trailing edge of the plate are also effects that are influencing the temperature measured on the plates.

Notice, that an increase of the flow velocity, it will disturb the equilibrium position, where the flow velocity (U) is balanced by the burning velocity (S_L),

$$U = S_L \tag{9}$$

The flame will be displaced upstream from the plate and consequently, heat and radicals will be lost. This is also will lead to lower value of the temperature read by IR camera. Naturally, the thermal conductibility ($\bar{k}_{cond}$) of the material presented in the flame holder will influence on the measured temperature. If the plate has higher $\bar{k}_{cond}$, the flame displacement will not be as significant as with a colder material (lower $\bar{k}_{cond}$).

As explained in Section 2.2.1, the temperatures measurements were performed in one pixel in the top side of the flame holder (see Figure 8).

The next two figures present the measured temperature profile from ϕ =0.7 to the flame extinction for a range flow velocities for Re=100-700. Figure 29 corresponds to the reference plate (SS), Figure 30 are related to the electrolyte A and electrolyte B samples.

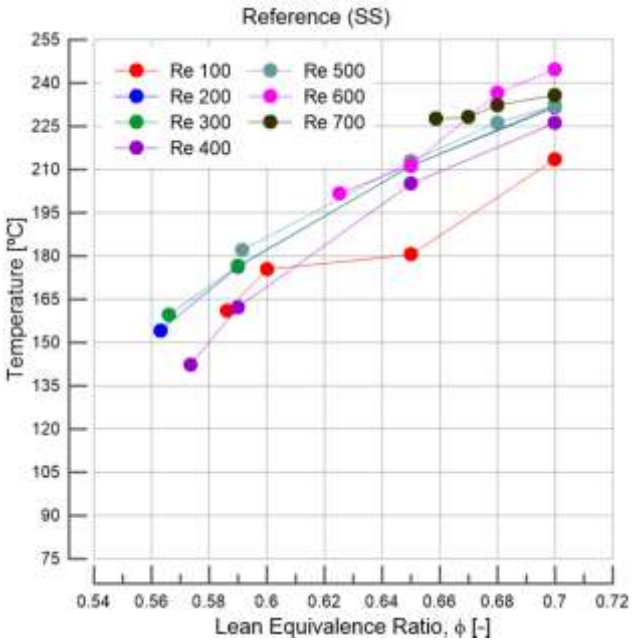

Figure 29 – Temperature evolution measured in the side of the stabilization SS plate (Reference) at lean conditions until blow-off limit.

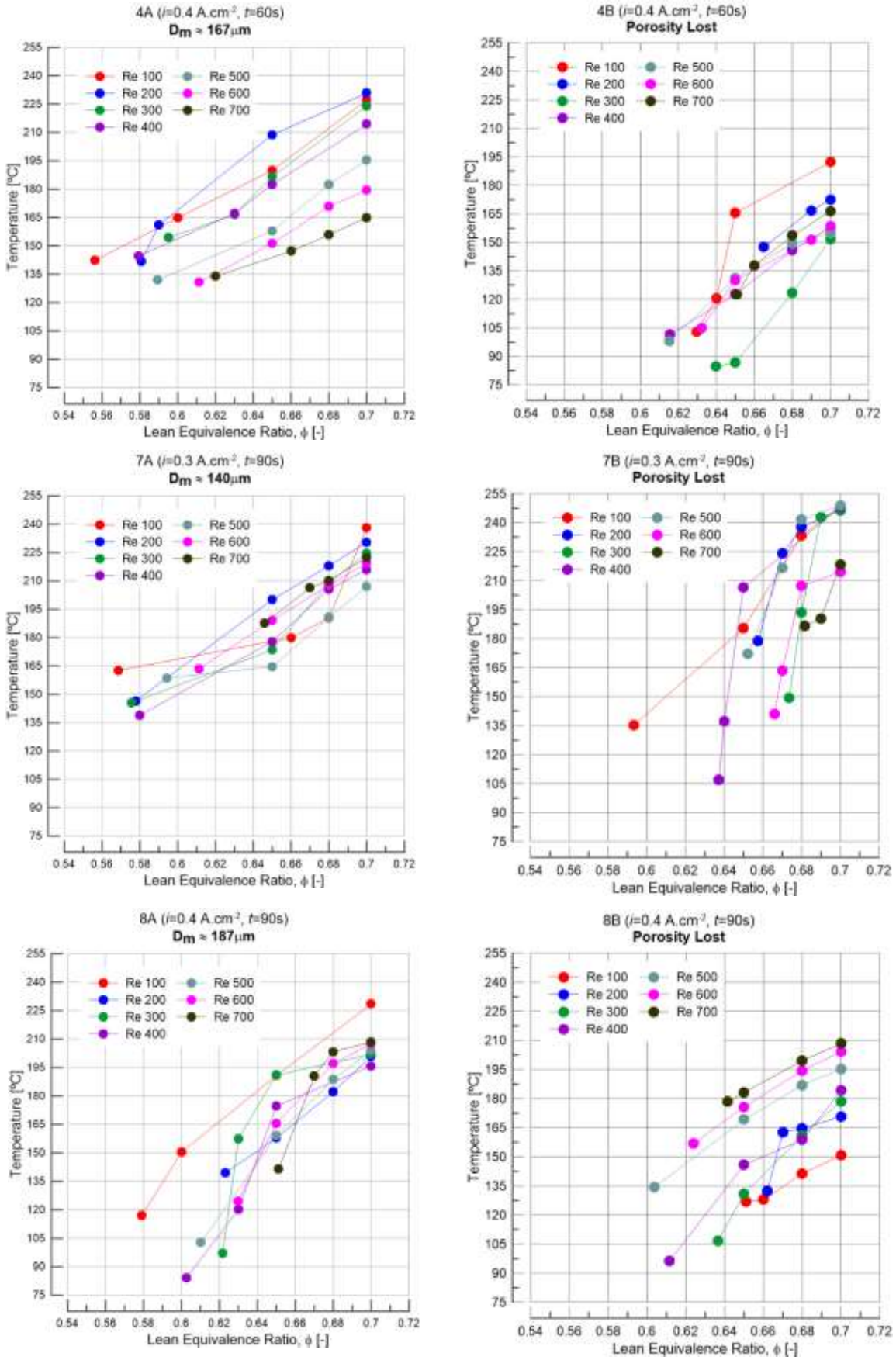

Figure 30 – Temperature evolution measured in the side of the stabilization plate at lean conditions until blow-off limit. The left side is regarding to the ZnO porous materials produced from Electrolyte A, and the right side corresponds to electrolyte B. The D_m values of electrolyte B were omitted because its porosity structure was lost.

The end left points for each line of flow velocity correspond to the near flame blow-off (BO) limit, i.e., $\phi = \phi_{BO} - 0.01$ as explained in the Stand-off Measurements section (Section 2.4).

Notice the temperatures for ZnO porous material 4A and 7A produced from electrolyte A (see Figure 30) and their stability diagrams shown in Figure 28. Observing the temperature results, this two ZnO materials are the samples that present a smoother/linear temperature variation along ϕ decrements. Oppositely, the remain samples have prominent slopes, with a noticeably reduction of the temperatures near the blow-off state. For instance, in the samples synthesized from electrolyte A (4A, 7A and 8A) and observing the Re 300 green curves, the temperature measured near blow-off limit for both 4A and 7A was around 150˚C, although for sample 8A this value drastically decreased to approximately 90˚C. Also, this temperature results for samples 4A and 7A are similar to the reference (Figure 29), corroborating the approach of the stability diagrams seen in Figure 28 of ZnO samples 4A and 7A to the reference.

Gathering this temperature and stability results, it is evident how important are the pores dimension in the flame stabilization, since materials with pores of a mean diameter of 167μm lead to a behaviour identical to the SS plate.

Moreover, the positive slope observed in all temperatures curves is the result of the join of the effects explain earlier in present topic: decrease of T_{ad} with ϕ, the heat and radical lost with the increase of flow velocity, and the $\bar{k}_{cond}$.

According Olorunyolemi et al. [41] which studied the thermal conductivity of a micrometre ZnO particle ($\bar{k}_{ZnO\ (\mu m\ particle)} \approx 0.1\ W/mK$ in a temperature range of 0-200˚C), it is possible to assume that the synthesized material has a smaller thermal conductivity relative to the SS ($\bar{k}_{SS} \approx 13 W/mK$ [42]). As ZnO has a smaller $\bar{k}_{cond}$, it is expecting a decrease of the temperature, as observed in Figure 30.

3.2.3 STAND-OFF DISTANCES – PECLET NUMBER

Figure 31 shows the stand-off distances measured at incipient blow-off. Towards lower flow velocities (Re between 100 and 300), the flame base reaches close proximity to the plate with the ZnO samples synthesized with electrolyte A (Figure 31(a)). This result can be attributed to the pores size, which their dimension may be inferred from the velocity field forcing the approximation of the flame seeking for stabilization. Also, it is observed a constant stand-off distance for the reference plate (nearly a vertical curve as seen in the black curve of Figure 31), which varies between 1.5 and 2.0 mm in either flow velocity. Regarding to electrolyte B (Figure 31(b)) the stand-off distances measured are stochastic, without showing a specific behaviour. For small Re, a displacement towards the flame holder has been observed, and for higher Re the flame is positioned a longer distance from the plate trailing edge.

In order to understanding which are the effects that are influencing the interaction between the flame base and the stabilization plate, it was computed a Peclet number (*Pe*) for this investigation, as carried out similar by Haber and Suntz [43]. Qualitatively *Pe* is defined as the ratio between the convection and conductive heat transfer of the air/methane mixture (control volume, CV, illustrated in Figure 33).

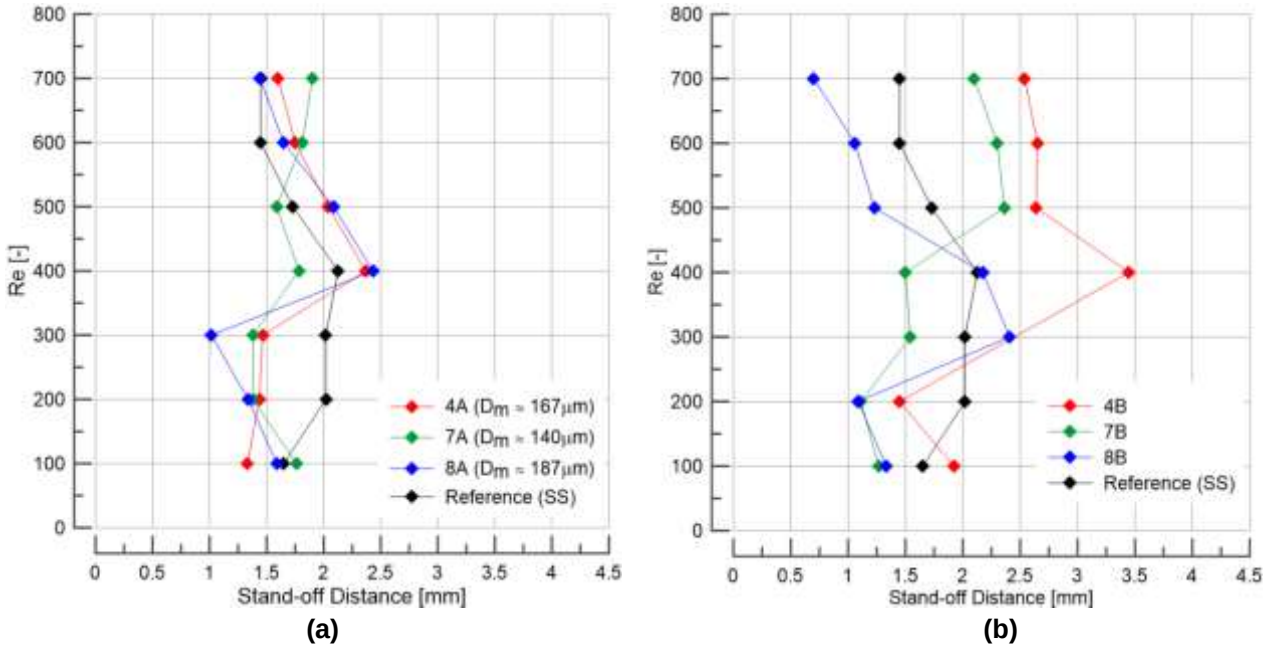

Figure 31 – Stand-off distances (d_s) measured near blow-off limit (a) electrolyte A (w/ KCl) and (b) electrolyte B (w/o KCl). The D_m values of electrolyte B were omitted because its porosity structure was lost.

The dimensionless Peclet number is defined as follow

$$Pe = \frac{d_s}{\delta_z} \tag{10}$$

where, d_s is the stand-off distance and δ_z is the Zeldovich thickness. This latter parameter, δ_z, was an arbitrary definition of flame characteristic thickness introduced by Zeldovich [44] and defined as follow

$$\delta_Z = \frac{\dot{k}/c_p}{\dot{\rho}_u S_L} \tag{11}$$

where S_L is the laminar flame velocity, $\dot{\rho}_u$ the unburned gas mass, $\dot{\kappa}$ the fuel-air mixture thermal conductivity and c_p the specific heat conductivity at constant pressure. S_L was determined according to study carried out by Trindade [44].

The results obtained for dimensionless *Pe* number are shown in Figure 32. As seen in Figure 32, the reference plate (black curve) *Pe* is always above 1, which means that the flow velocity U is governing the condition of blow-off. However, looking at the porous material curves (coloured lines), for lower flow velocities (Re<300, i.e., U<1.3m/s) the heat transfer by conduction begins to have the same role on the blow-off limit and compete with the advection form.

The *Pe* curves of ZnO materials synthesised from electrolyte A (Figure 32(a)) can be justified by the pores dimensions, since it might influence the velocity gradient that is achieved at the trailing edge of the plates. Note that the ZnO deposit with the smallest pores (7A, D_m=140μm) is the one that

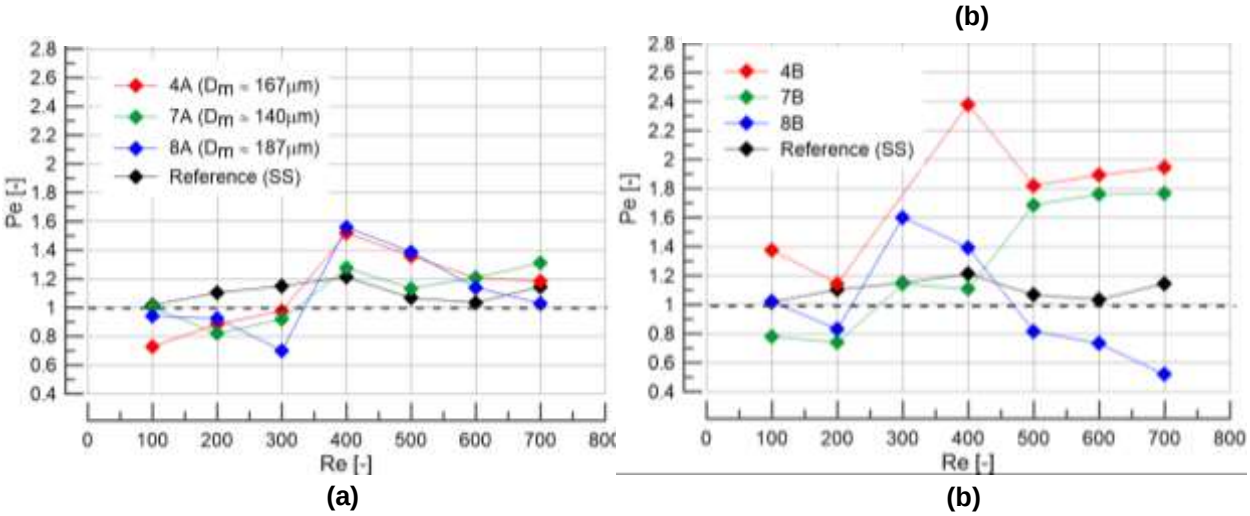

Figure 32 – Stand-off Peclet numbers ($Pe=d_s / \delta_Z$) for produced material with (a) electrolyte A (w/ KCl) and (b) electrolyte B (w/o KCl).

slightly approximates to the reference stability diagram (Figure 28(a)). According to study carried out by Leitão [45], an almost constant velocity profile is reached through the porous material independent of the tested flow rates ($\bar{U} = 0.1$ m/s), which can help to understand the flame performance with this type of media. In fact, it is possible to conclude that this material (green curve in Figure 32(a)) is an extension of the SS. Summarizing, materials with a pores with a mean diameter of 140µm don't create instabilities to the flame, which might suitable to work as support catalysts in future applications.

Contrarily, the obtained results with the larger pores (as material 8A, D_m=187µm) shown in Figure 32(a), demonstrated that this type of materials creates a resistance to the passing flow, leading to a decrease of flow velocity at the trailing edge of the flame holder. Consequently, the flame approaches the surface, and the heat loss from the flame to the plate increases, leading to the flame extinction. Note that this assumption is only valid for low mixture velocities (until approximately Re=300), since with higher *U* the stability diagram of all ZnO porous material approaches the reference curve (Figure 28(a)). Towards to higher Re the mixture goes around the deposited material, providing the same conditions as SS plate, i.e., velocity field at the trailing edge of the plate as the reference (SS plate).

It was not possible to evaluate the velocity field using particle image velocimetry (PIV) measurements, because of the possibility of alumina (Al_2O_3) particles being deposited in the pores and consequently affecting the velocity profile. In fact, this is an empirical assumption based on the obtained results.

Regarding to the material produced with electrolyte B (Figure 32(b)) it was not possible to realise an explanation for its behaviour, since all the samples have lost completely their porosity structure after experiments on the burner.

3.2.4 HEAT FLUX

In order to assemble all the experimental results and explain about the mechanism that is behind the flame blown-off in lean conditions, an energy balance at the control volume (CV) in Figure 33 were carried out.

$$\frac{dE}{dt} = \dot{Q}_F - \dot{Q}_S + \dot{m}_{in}h_{in} - \dot{m}_{out}h_{out} \tag{12}$$

in which $\dot{Q}_F$ is the heat transfer that enters into CV coming from the flame, $\dot{Q}_S$ is the heat loss to the plate surface and $\dot{m}_{in}h_{in} - \dot{m}_{out}h_{out}$ is the difference of rate of energy into the CV accompanying the mass flow.

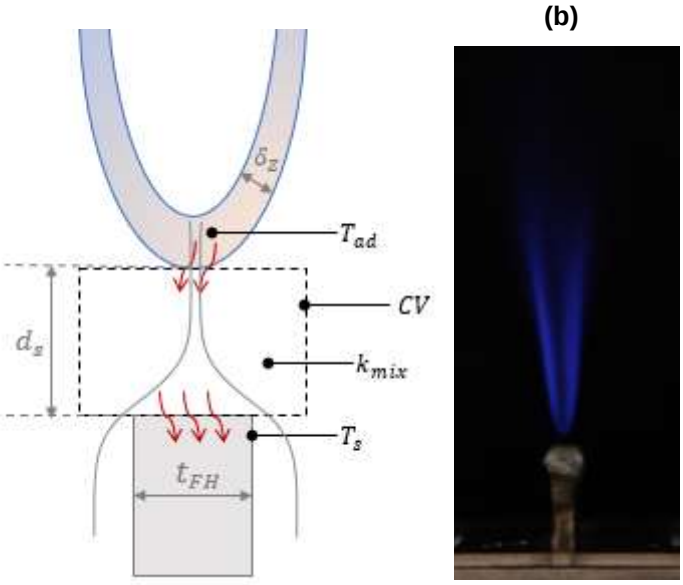

Figure 33 – (a) Schematic representation of the flame stabilization at the plate trailing edge at incipient blow-off where T_{ad} is flame adiabatic temperature, T_s the surface temperature (pixel as shown in Figure 8), k_{mix} the thermal conductivity of the Ch_4/air mixture, d_s the stand-off distance, and δ_Z the Zeldovich flame thickness and t the plate thickness. (b) Moment near blow-off limit for sample 4A (D_m=167μm) at Re=300.

Concerning to the material where the flame is stabilized, the amount of energy that is being transferred by conduction (Q) and unit of time is known as Fourier's Law [24],

$$Q'' = k\frac{dT}{dx} \tag{13}$$

Where, Q'' is the rate of heat transfer per unit area (W/m^2), k is the SS or ZnO thermal conductivity, and dT/dx corresponds to the temperature gradient. Simplifying it is possible to assume the flame as a hot

source that is heating the stabilization plate. Thus, combining previous Equations (12) and (13), the heat flux that is passing to the flame holder near to blow-off limit is state as follow,

$$\dot{Q} = t_{FH} k_{mix} \frac{T_F - T_S}{d_s} \tag{14}$$

where, $\dot{Q}$ is the heat flux, t_{FH} is the flame holder thickness, k_{mix} the thermal conductivity of fuel-air mixture, T_F is the flame adiabatic temperature, T_S the temperature of the plate surface and d_s is the stand-off distance. Note that T_F=T_{ad} was performed using Cantera code over GRI-Mech 3.0 and k_{mix} calculated according to gas proprieties found in literature [24,47].

Figure 34 shows the obtained heat fluxes for the synthesized porous ZnO material and for the reference plate (without material deposited).

Looking at equation (14) it is clear that the last term is the only parameter that may influence the heat fluxes, which is the quotient of the temperatures difference and the stand-off distance, since the other two parameters remain nearly constant (k_{mix} variation with ϕ is negligible when compared with T_F, T_S and d_s).

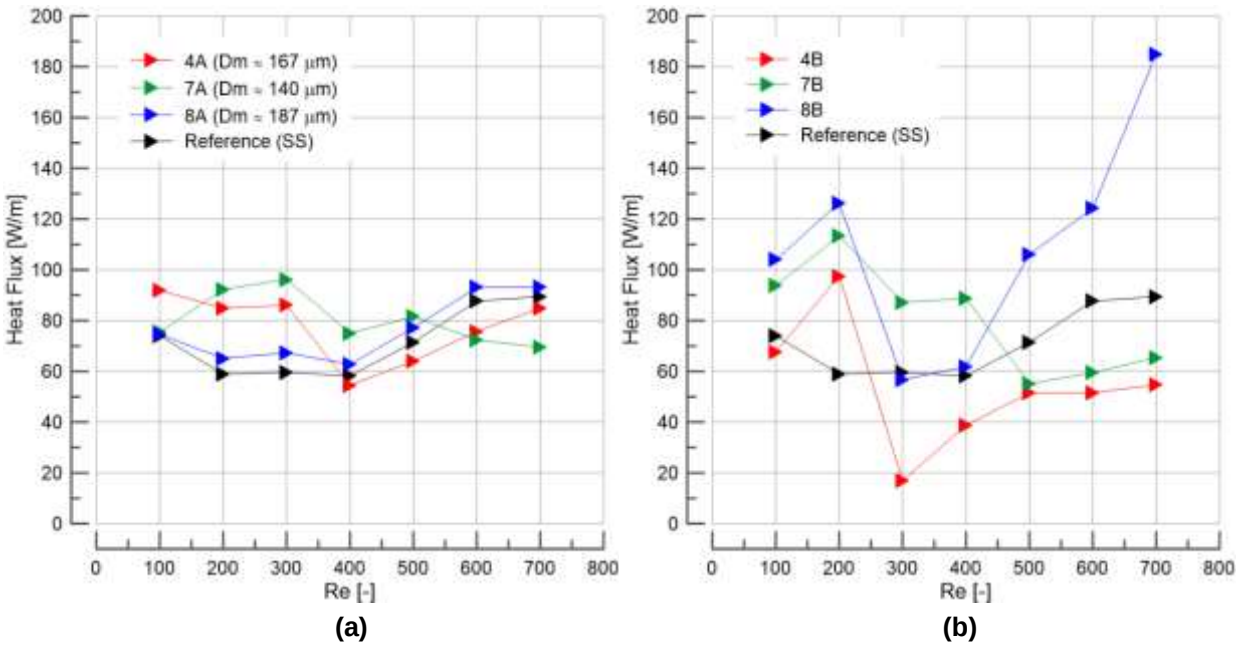

Figure 34 – Heat fluxes measured at incipient blow-off for the produced material with (a) electrolyte A (w/ KCl) and (b) electrolyte B (w/o KCl).

Assessing the black line behaviour shown in Figure 34, which corresponds to the SS plate, the heat losses from the flame base to the plate increases slightly with increasing of U at near state of blow-off. As the *U* increases (above Re =400) the flame extinguishes for higher values of ϕ as seen in stability diagrams (Figure 28). Consequently, the T_{ad} increases, the numerator of the quotient mentioned previously also increases and subsequently the conductive heat losses for the plate increase. Also, it was observed an approximation of the flame to the plate (as shown in Figure 31) which also increase the heat losses to the flame holder.

Regarding to electrolyte A, Figure 34(a), its observed a opposite behaviour of the ZnO material relative to the reference curve for lower flow velocities. Below Re = 400 the heat losses are higher than the reference (e.g. for Re=300, $\dot{\mathrm{Q}}_{\mathrm{Reference}} = 60\ \mathrm{W/m}$ and $\dot{\mathrm{Q}}_{7\mathrm{A}} \approx 100\ \mathrm{W/m}$). Also, it was observed a displacement of the flame towards the plate (see green curve in Figure 31), which increase the heat transfer to the plate. Notice that the higher $\dot{Q}$ values obtained for the porous material with small pores (7A, with D_m=140µm) might be assigned to the thermal conductivity of this type of material. As mentioned in Section 3.2.2, ZnO material has $\bar{k}_{ZnO\ (\mu m\ particle)} \approx 0.1\ W/mK$ in a temperature range of 0-200˚C and the SS plate has $\bar{k}_{SS} \approx 13 W/mK$.

For higher *U*, the $\dot{Q}$ curves of the ZnO material approach the reference line, producing the same effect as the SS plate in flame stabilization, as confirmed by the stability diagrams shown in Figure 28(a).

The reported results for the reference's heat flux might be contribute for evaluation the blow-off limits concerning to the inverted flames. In the Re range of 200-400 the heat transfer is nearly unaltered (about 60W/m), which lead to the conclusion that the flame is blown off at characteristic heat losses to the plate, a detail that should be not neglect when studying the mechanisms that might influence the state of blow-off.

Analysing Figure 34(b), it is observed that the heat flux doesn't follow any specific tendency, since the material produced with electrolyte B created a weak structure that loses its morphology. The minor value of $\dot{Q}$ measured for sample 4B at Re=300 (red curve) is due to the significant stand-off distances measured at this condition. The inconstant curves behaviour is result of the combination of the fluctuations observed in the stability diagrams (Figure 8) and the flame displacements (Figure 31).

CHAPTER 4

CONCLUSIONS

4.1 SUMMARY OF CONTRIBUTIONS

The main goal of this investigation was to analyse the influence of a porous structure in the stabilization of a V-shaped flame. Porous materials are found in micro and catalysis combustion, since they are used as the material that is impregnated with the catalysts, known as support material. To this end, it was synthesised porous morphologies suitable to use in a twin-slit burner, in order to perform combustion experiments with inverted flames. These porous materials (ZnO) were produced by electrodeposition technique. Consequently, two main investigations were accomplished in the present study.

The first one was analysing which are the electrodeposition conditions that allows to produce 3D interconnected porous materials, and also infer about the electrolyte composition that fabricate firmer structures that could be work as support material. This chemical study contemplated detailed chemical and physical characterization over the all produced samples, which included XRD and SEM techniques (presented in the section 3.1).

Presence of a porous material in the flame holder contemplated the second part of this study. Temperature measurements with a thermographic camera and the stand-off distances were dramatically important to assess about the influence of different pores size (in a range of 140 to 187 μm) in the flame behaviour, and also to evaluate the heat flux that it's transferred from the flame to the plate.

The experimental results fit into the hypothesis in which the pores size of the synthesized material changes the velocity profile at the trailing edge of the flame holders, particularly for small flow velocities.

Concerning to the synthesized ZnO material, the main conclusions are summarized and listed bellow:

(i) Higher density currents (*i*) and electrodeposition times (*t*) provides the synthetisation of porous materials;

(ii) Longer electrodeposition times leads to a creation of a material with bigger pores. This was justified by the increase of the bubbles density that occurs in such condition and concluded with the image treatment performed in SEM micrographs (explained in section 2.7 and presented in section 3.1.3);

(iii) The importance of KCl in the electrolyte solution was evaluated, showing that this is an important parameter to produce a stronger and resistant porous structure to perform tests in this type of twin-slit burners. The samples produced with the electrolyte solution without KCl lost completely its porous morphology, as concluded in section 3.1.4.

Regarding to combustion experiments, the main conclusions to be drawn with the surface manipulation at incipient blow-off of an inverted flame may be summarized as follows:

(i) A material with small pores (mean diameter of 140 μm) behaves as a clean flame holder (no material deposition) given the similarities in the stability curves (Figure 28).

(ii) The presence of a porous media does not promote any change of the flame stabilization for higher mixture velocities, since the flow does not seem to travel through the porous material.

(iii) The presence of a porous media changes the velocity profile at the trailing edge of the plate since a displacement of the flame occurs towards the flame holder, consequently increasing the heat transfer from the flame base to the stabilization plate, and leading to the flame blown off.

(iv) With a porous material and for low flow velocities the conductive heat transfer is governing the flame stabilization, given that a $Pe<1$ was measured. This fact corroborates the influence of the pores dimension on the velocity profile.

4.2 GUIDELINES FOR FUTURE WORK

The work developed opened a new view of the potential application of porous surfaces in water home heating devices as for example, in multiple-slit burners. The results obtained provided a first understanding how pores dimension might influence the flame behaviour, leaving possible research topics and improvements. These are listed next:

(i) Produce porous materials with a diameter in the range of 140 µm or lower, in order to infer about the pores diameter influence, and eventually find an ideal dimension that allows a greater flame stability;

(ii) Perform the same experiments and measurements but with a different a material with a thermal conductibility similar to the SS plate;

(iii) A research over a porous structure (with a mean diameter of 140µm) but with an methane catalysts impregnation:

(iv) Perform the experiments tests with a smaller plate thickness (t_p<3 mm) and assess about the temperature profile along the plate.

In all the future works based on this study, it is desirable proceed to the removal of material deposited in the lateral sides of the SS plates. Ideally, should exist only material on the face where the flame is anchored, because it's in that zone where all the phenoms governing the flame sustainability are occurring,

REFERENCES

[1] M.L. Williams and D.C. Carslaw. New Directions: Science and policy – Out of step on NO x and NO 2?, *Atmospheric Environment* 45: 3911–3912, 2011.

[2] D. Dunn-Rankin and P. Therkelsen. *Lean Combustion, Technology and Control*. Academic Press, 2nd edition, 2016.

[3] Y. Ju and K. Maruta. Microscale Combustion: Technology development and fundamental research. *Progress in Energy and Combustion Science*, 37(6): 669-75, 2011.

[4] Y. Nakamura, J. Gao and T. Matsuoka. Progress in small-scale combustion. *Journal of Thermal Science and Technology*, 12(1): 1-28, 2017.

[5] B. Bui. Micro-scale combustion issues and approaches. MSc thesis, California State University, 2013.

[6] J.H. Lee and D.L. Trimm. Catalytic combustion of methane. *Fuel Processing Technology*, 42: 339-359, 1995.

[7] T. Heppenstal. Assessment of the impact of catalytic surface combustion on heat transfer in a tube. *Heat Recovery Systems & CHP*, 13(6): 483-492, 1993.

[8] S. Govender and H.B. Friedrich. Monoliths: A Review of the Basics, Preparation Methods and Their Relevance to Oxidation. *Catalysts*, 7(62), 2017.

[9] S. Parmentier, M. Braack, U. Riedel and K. Warnatz. Modeling of combustion in a lamella burner. *Combustion Science and Technology*. 175(1): 185-206, 2003.

[10] T. Lúcio. Rich-Lean Flame Interaction on a Lamella Type Burner. MSc Thesis, Lisbon University, 2015.

[11] B. Lewis and G. Von Elbe, Stability and Structure of Burner Flames, *J. Chem. Physics*, 11: 75-97, 1943

[12] H. Edmondson and M.P. Heap. Blowoff of Inverted Flames, *Combust. and Flame*, 14: 191-194, 1970.

[13] S.R. Vaillant and A.S. Gastec. Catalytic combustion in a domestic natural gas burner, *Catalysis Today*, 47: 415-420, 1999.

[14] S. Specchia and G. Toniato. Natural Gas Combustion Catalysts for Environmental/friendly Domestic Burners, *Catalysis Today*, 147(2): 99-106, 2009.

[15] G.A. Lange. Design of new Cu-Fe metallic oxide foams formed by electrodeposition for asymmetric supercapacitors electrodes. MSc Thesis, Lisbon University, 2014.

[16] M. Willander, Q. X. Zhao, Q.-H. Hu, P. Klason, V. Kuzmin, S. M. Al-Hilli, O. Nur and Y.E. Lozovik. Fundamentals and properties of zinc oxide nanostructures: Optical and sensing applications, *Superlattices and Microstructures*, 43: 352-361, 2008.

[17] A. B. Djurišić, A. M. M. Ng and X. Y. Chen. ZnO nanostructures for optoelectronics: Material properties and device applications, *Progress. in Quantum Electronics*, 34(4): 191-259, 2010.

[18] Z. L. Wang. Nanostructures of zinc oxide, *Materials Today*, 7(6): 26-33, 2004.

[19] L. Xu, Y. Guo, Q. Liao, J. Zhang and D. Xu. Morphological Control of ZnO Nanostructures by Electrodeposition, *J. Phys. Chem. B*., 109(28): 13519-13522, 2005.

[20] R. Tena-Zaera, J. Elias, G. Wang and C. Lévy-Clément. Role of Chloride Ions Electrochemical Deposition of ZnO Nanowire Arrays from O2 Reduction, *J. Phys. Chem. C*, 111(45): 16706-16711, 2007.

[21] Z. Fan and J. G. Lu. Zinc Oxide Nanostructures: Synthesis and Properties, *Journal of Nanoscience and Nanotechnology*, 5(10): 1561-1573, 2005.

[22] B.J. Plowman, L. A. Jones and S.K. Bhargava. Building with bubbles: the formation of high surface area honeycomb-like films via hydrogen bubble templated electrodeposition, *Chem. Commun*., 51: 4331-4346, 2015.

[23] P.D.F.Pontes. Thermographical analysis of interface heat transfer mechanisms, with high temporal resolution. MSc Thesis, Lisbon University, 2016

[24] F.P. Incropera, D.P.Dewitt, T. L. Bergman and A.S Lavine. Fundamentals of Heat and Mass Transfer, 6th ed., John Wiley & Sons, Hoboken.2007.

[25] C.J.Sung, C.K Law and A.Umemura. 1992. On Adiabatic Stabilization of Inverted Flames, *Proc. Combust. Inst*., 24: 205-212, 1992.

[26] Y. Shoshin and L.P.H De Goey. On the Correlation of Inverted Flame Blow-Off Limits with the Boundary Velocity Gradient at the Flame Holder Surface, *Combust. Explo. And Shock Waves*, 5: 520-527, 2015.

[27] http://rruff.info/Sylvite (May 2018).

[28] http://rruff.info/Zincite (May 2018).

[29] http://www.xenics.com/pt/application/c%C3%A2meras-lwir-termogr%C3%A1ficas-n%C3%A3o-refrigeradas (October 2018)

[30] https://fenix.tecnico.ulisboa.pt/investigacao/ist-nm/low-temperature-and-high-magnetic-field-laboratory (October 2018)

[31] R.C. Gonzalez and R.E. Woods, Digital Image Processing Pearson Education Inc., 2nd Edition. 2008.

[32] https://www.mathworks.com/company/newsletters/articles/the-watershed-transform-strategies-for-image-segmentation.html. (May 2018).

[33] E. W. Lemmon, R. T. Jacobsen, S. G. Penoncello, and D. G. Friend. Thermodynamic properties of air and mixtures of nitrogen, argon, and oxygen from 60 to 2000 k at pressures to 2000 mpa. Journal of physical and chemical reference data, 29(3):331–385, 2000

[34] M. C E. Manuel, S.P Lin 1, W.H. Lu and P.T. Li. Errors in Thermographic Camera Measurement Caused by Known Heat Sources and Depth Based Correction, AUSTM, 6(1): 5-12, 2016.

[35] Scott A. S. Introduction to X-Ray Powder Diffraction Data Analysis. http://prism.mit.edu/xray/. (May 2018)

[36] A. Moezzi, M. Cortie and A. McDonagh. Transformation of zinc hydroxide chloride monohydrate to crystalline zinc oxide, *Dalton Trans*., 45, 7385-7390. 2016

[37] R, Tena-Zaera, J. Elias, C. Lévy-Clément, C. Bekeny, T. Voss, I. Mora-Seró and J. Bisquert. Influence of the Potassium Chloride Concentration on the Physical Properties of Electrodeposited ZnO Nanowire Arrays, *J. Phys. Chem*., 112: 16318-16323. 2008

[38] https://pubchem.ncbi.nlm.nih.gov/compound/potassium_chloride#section=Top (May 2018).

[39] C. Trevino, S. Donnerhack and N. Peters. LDA Measurements in the premixed V Flame Stabilized in the Wake of a Flat Plate Boundary Layer, *Comb. And Flame*, 8: 505-510, 1991.

[40] P. Coelho and M. Costa. Combustão. Edições Orion, 1 st edition, 2007

[41] T. Olorunyolemi, A. Birnboim , Y. Carmel, Jr. O.C. Wilson and I.K. Lloyd. Thermal conductivity of Zinc Oxide: From Green to Sintered State, *J. Am. Ceram. Soc*., 85, 1249-1253, 2002.

[42] Y.A. Çengel and A. F. Ghajar A.F. Heat and Mass Transfer, Fundamentals & Applications, McGraw-Hill, New-York, 5th ed., 2015.

[43] T. Haber and R. Suntz R. Effect of different wall materials and thermal-barrier coatings on the flame-wall interaction of laminar premixed methane and propane flames, *Int. J. Heat and Fluid Flow*: 69, 95-105, 2018.

[44] T. Trindade. Chemiluminescence spectral identity of premixed methane and propane flames. Phd Thesis, Lisbon University, 2015

[45] I. Leitão. Experimental and Analytical Flame Transfer Functions of Multi-Perforated Plate Burners. MSc Thesis, Lisbon University, 2009.

APPENDIX

MATLAB – IMAGE TREATMENT (PORES DIAMETER)

```
clc;clear; close all;
readImage=imread('4.tif');

binaryImage=imbinarize(readImage,graythresh(readImage));
bw=bwareaopen(~binaryImage,60);
D = -bwdist(~bw);
minimize_overlap = imextendedmin(D,2);

%imshowpair(bw,mask,'blend')
D1 = imimposemin(D,minimize_overlap);
Ld=watershed(D1);
bw2=bw;
bw2(Ld==0)=0;

Pore_Size=bwareaopen(bw2,630);

Table=regionprops('Table',Pore_Size,'Area','EquivDiameter','Eccentricity');

figure(1)
imshowpair(readImage,Pore_Size,'blend');
figure(2)
imshowpair(readImage,Pore_Size,'Montage');
figure(3)
imshow(binaryImage)
```

MATLAB – IMAGE PLOTTING (PORES DIAMETER)

```
clc;clear;close all;
load('4Test.mat');
D2=Table(:,3);
D1=table2cell(D2);
DiameterPix=cell2mat(D1);

Conversion=900/371; %micro/pixel
MeanDiameter=mean(DiameterPix)*Conversion;
Diameter=DiameterPix*Conversion;
standard_deviation=std(Diameter);

xmin=min(Diameter);
xmax=max(Diameter);

TotalCount=length(Diameter);
```